Acta Neuropathologica Communications

RESEARCH

Open Access

Cellular signatures of melanocortin pathway genes across the locus coeruleus

Alisha Basak[1,2†], Fahrünisa Meryem Betül Erol[1,2†], Maria Caterina De Rosa[1,2], Zhangji Dong[2,3], Victor Ogbolu[4], Hannah J. Glover[1,2], Rick Rausch[1,2], Gunnar Hargus[5], Jordi Creus-Muncunill[6], Heather Buchanan[5], Yu Bai[6], Qi Su[6], Betty Chang[6], Christina Adler[6], Delaney Flaherty[5,7], Benjamin Ciener[5,7], Harrison Xiao[5,7], Hasini Reddy[5,7], Pascaline Aime-Wilson[6], Christiane Reitz[8], Mark W. Sleeman[6], Judith Y. Altarejos[6], Rudolph L. Leibel[1,2], Liang Oscar Qiang[4], Andrew F. Teich[5,7] and Claudia A. Doege[2,5*]

Abstract

Obesity and Alzheimer's disease (AD) are epidemiologically associated. The locus coeruleus (LC)—the brain's primary and most significant source of norepinephrine—is one of the earliest sites of neurodegeneration in AD. The LC participates in feeding behavior through connections with the hypothalamus. The cellular composition of the LC has been characterized at single-cell resolution. However, the constituent cellular signatures of genes related to energy homeostasis—such as the melanocortin pathway genes—in the LC are unclear. We performed single-nucleus RNA sequencing and spatial transcriptomics (Visium) in the human LC, and HiPlex RNAscope in the LC of mice. The melanocortin pathway gene *MRAP2* was expressed in the majority of DBH neurons across the LC. *Mrap2* was also co-expressed with AD-associated genes such as *App*, *Psen1*, *Psen2*, and *Sorl1*. More than 20% of Dbh neurons in the LC were positive for *Mrap2*, *App*, *Psen1*, and *Psen2*. *Mrap2* is expressed in the central nervous system and modulates the trafficking and signaling of all five G-protein coupled receptors (GPCRs) of the melanocortin receptor family: Mc1r, Mc2r, Mc3r, Mc4r, and Mc5r. In mice, among the melanocortin receptors, *Mc5r* showed the highest co-expression with *Mrap2*, accounting for 17.9% of *Mrap2*-positive cells, followed by *Mc2r* with 10.9% of *Mrap2*-positive cells. *Mc1r*, *Mc3r*, and *Mc4r* showed very limited co-expression with *Mrap2*. Our study reveals that many *Mrap2*-positive cells do not express any melanocortin receptor genes, warranting future studies into metabolically relevant GPCRs downstream of MRAP2 in the LC. In summary, our study characterizes melanocortin molecular substrates in the human and mouse LC and highlights *MRAP2* as a potential link between pathways of energy homeostasis and neurodegeneration.

Keywords Locus coeruleus, Melanocortin pathway, Alzheimer's disease, Food intake, Obesity, Energy balance

†Alisha Basak and Fahrünisa Meryem Betül Erol have contributed equally to this work.

*Correspondence:
Claudia A. Doege
cad2114@cumc.columbia.edu

Full list of author information is available at the end of the article

Introduction

Epidemiological and experimental studies have identified links between obesity and Alzheimer's disease (AD), with obesity increasing the risk of AD [1–5]. Disruption of the locus coeruleus (LC) system is associated with neurodegenerative diseases such as AD [6]. The LC is a small brainstem nucleus located within the dorsal wall of the rostral pons, in the lateral floor of the fourth ventricle. It is the brain's major source of norepinephrine (NE). LC NE neurons innervate both cortical and subcortical structures including the cerebellum, basal telencephalon, thalamus, amygdala, and hypothalamus [7]. Accordingly, LC NE neurons play a role in many physiological and behavioral processes including arousal, attention, memory, cognition, stress response, activity of the sympathetic nervous system, and energy homeostasis [8–14].

The LC is among the earliest brain regions to exhibit tau pathology in AD, with progressive loss of LC neurons evident as the disease advances [15–17]. Aberrant accumulation of hyperphosphorylated tau has been reported in LC neurons in addition to its presence in the hypothalamic tuberomammillary nucleus (TMN) [18]. While the most recognizable feature of AD is memory impairment, non-cognitive symptoms of AD such as sleep disorders, autonomic dysfunction, and endocrine alterations may be influenced by disruption of communication between the LC and hypothalamus [19, 20]. The hypothalamus is the "master regulator" of homeostatic functions, including energy homeostasis, sympathetic and parasympathetic activities, and sleep–wake cycles [21].

Both inputs to the LC from the hypothalamus and outputs from the LC to the hypothalamus have been reported [22]. Unidirectional projections from the TMN to the LC mediate the sleep–wake cycle [23–26]. Bidirectional neuronal projections to the LC arising from the ventrolateral preoptic nucleus (VLPO), suprachiasmatic nucleus (SCN), dorsomedial nucleus (DMH), and paraventricular nucleus (PVN) regulate arousal and the sleep–wake cycle [24, 27–29]. Additionally, there are afferent connections to the LC from the PVN of the hypothalamus involved in the coordination of the stress response [30–32]. Of note, there are bidirectional connections between the lateral hypothalamus (LH) and LC that regulate arousal and wakefulness, and may also play a role in the NE-mediated suppression of feeding via beta-adrenoceptors [27, 33–37].

LC NE activity, assessed via in vivo fiber photometry calcium imaging, optogenetics, and chemogenetics, is enhanced during food approach and progressively suppressed during food consumption, suggesting that LC responses to food are modulated by satiety state. Visual-evoked NE activity in LC neurons is attenuated in sated mice, suggesting that satiety modulates NE encoding of multiple behavioral states. Furthermore, food intake is reduced by brief or longer durations of NE activation in LC neurons and stimulation of LC neurons projecting to the LH suppresses feeding in mice [14]. While hypothalamic feeding circuitry is interconnected with the NE neurons of the LC, further investigation of the molecules that mediate this feeding response in LC NE neurons is necessary.

Previous studies on metabolically relevant G-protein coupled receptors (GPCRs), including hypocretin receptor 1 (OX1R), growth hormone secretagogue receptor (GHSR), and melanin concentrating hormone receptor 1 (MCHR1), revealed their expression patterns in the LC and function conveyed by LC NE neurons [38–46]. Furthermore, hypothalamic and brainstem adrenocorticotrophic hormone (ACTH)- and alpha-melanocyte-stimulating hormone (α-MSH)-containing fibers are present in the rat LC [47, 48]. ACTH is a ligand for melanocortin 1 receptor (MC1R) and melanocortin 2 receptor (MC2R) [49, 50]. α-MSH, as derived from proopiomelanocortin (POMC), is a ligand at MC1R, melanocortin 3 receptor (MC3R), melanocortin 4 receptor (MC4R), and melanocortin 5 receptor (MC5R) [51, 52]. The role of α-MSH as an anorexigenic peptide at MC4R has been studied in the hypothalamus [53]. Expression of *Mc4r* has been reported in the LC of rodents [54–58]. The melanocortin receptor genes and their ligands are part of the leptin-melanocortin pathway, which also includes the *leptin receptor* (*LEPR*) and the *melanocortin 2 receptor accessory protein 2* (*MRAP2*) [59, 60]. In the hypothalamus, neurons of the leptin-melanocortin pathway participate in energy homeostasis by regulating food intake and energy expenditure [61]. The adipokine leptin has central effects mediated by the hypothalamic leptin-melanocortin pathway and its projections to various parts of the brain. Hyperleptinemia and obesity have been associated with AD risk [62]. Whether the effects of NE neurons on feeding are conveyed by the leptin-melanocortin pathway is unknown [63–65]. Further molecular characterization of the LC is required to identify how NE neurons contribute to the pathways of energy homeostasis [63–66].

Genetic, molecular, and clinical evidence established the roles of *amyloid beta precursor protein* (*APP*), *presenilin 1* (*PSEN1*), *presenilin 2* (*PSEN2*), *sortilin related receptor 1* (*SORL1*), *apolipoprotein E* (*APOE*), and *triggering receptor expressed on myeloid cells 2* (*TREM2*) in AD pathogenesis [67–72]. APP mediates proteolytic processing of amyloid beta (Aβ) peptides that may accumulate in amyloid plaques, a pathological hallmark of AD. Mutations in *APP* cause autosomal dominant early-onset AD, providing direct causal evidence for its role in disease [68–70, 73]. *PSEN1* and *PSEN2* encode presenilin-1 and presenilin-2, the catalytic components of the γ-secretase complex that cleaves APP. Pathogenic mutations in *PSEN1* and *PSEN2* alter Aβ production

and cause familial early-onset AD [68, 70, 74]. *SORL1* encodes a neuronal sorting receptor involved in APP trafficking. Reduced *SORL1* expression or loss-of-function variants shift APP processing toward the amyloidogenic pathway, increasing Aβ generation. Genetic variants in *SORL1* have been associated with both early- and late-onset AD [75–77]. *APOE* is the strongest genetic risk factor for late-onset AD. *APOE* influences Aβ aggregation and clearance, lipid transport, and neuroinflammation, making it a central modulator of AD susceptibility [70, 72, 78]. *TREM2* encodes a microglial receptor involved in immune response and phagocytosis. Rare coding variants in *TREM2* substantially increase the risk of late-onset AD, highlighting the importance of microglial dysfunction and neuroinflammation in disease progression [79–82]. Molecular characterization is warranted to examine co-expression of melanocortin and these AD-associated genes in the cellular populations of the LC.

Here, we characterize the cellular and molecular components of the melanocortin pathway within the LC in humans and mice. Using single-nucleus RNA sequencing (snRNA-seq) and spatial transcriptomics in human postmortem LC tissue, in conjunction with RNAscope HiPlex across the mouse LC, we achieved single-cell resolution of melanocortin gene expression. Our findings reveal substantial co-expression of melanocortin and AD-associated genes in LC cellular populations.

Materials and methods

Human postmortem samples

Postmortem human metencephalon tissue from deidentified neurotypical donors was obtained from the New York Brain Bank, Columbia University, New York. Briefly, sequential transverse slices of the hemi-brainstem of 0.3 cm thickness were obtained. The LC was identified via its distinct dark blue pigmentation. Slices were frozen in dry ice, transferred to a sealed bag, and stored at − 80 °C until further use. For snRNA-seq, we sourced the LC region from a 74-year-old female donor. For spatial transcriptomics, slices of the LC region were sourced from a 76-year-old female donor.

Single nuclei isolation for snRNA-seq

The nuclei isolation protocol was adapted from 10 × Genomics. To isolate the region of interest, slices were briefly transferred to a Petri dish on ice, and great care was taken to include all of the visible LC using a 2 mm diameter punch. The punched tissue was immediately transferred to a 1.5 ml microcentrifuge tube containing 500 µl of pre-chilled Lysis Buffer (10 mM Tris–HCl, Millipore-Sigma #T2194; 10 mM NaCl, Millipore-Sigma #59222C; 3 mM $MgCl_2$, Millipore-Sigma #M1028; 0.1% Nonidet P40 Substitute, Millipore-Sigma #74,385), homogenized by gently moving up and down a Pellet Pestle 15 times and centrifuged for 3 s at 300 g at room temperature. The supernatant was collected in a new 1.5 ml microcentrifuge tube and centrifuged for 5 min at 850 g at 4 °C. The supernatant was removed, and the pellet was washed twice in 1 ml of Nuclei Wash & Resuspension Buffer (0.04% BSA, Sigma-Millipore #SRE0036, in PBS, Gibco # 10010023). After the second wash, the nuclei suspension was passed through a 40 µm Flowmi Cell Strainer (Bel-Art #H13680-0040) and centrifuged for 5 min at 300 g at 4 °C. The nuclei pellet was resuspended in Nuclei Wash & Resuspension Buffer and immediately loaded onto the 10 × Chromium instrument (Single Cell Analysis Core at Columbia University).

Sequencing libraries were generated using 10 × Genomics Chromium Single-Cell 3' Reagent Kit v3.

Human LC tissue processing for 10 × Genomics Visium spatial transcriptomics

Frozen samples were embedded in O.C.T. compound (Thermo Fisher Scientific, 23730571) and placed in dry ice to flash-freeze. A total of five 10-µm thick sections (2 consecutive sections from the rostral slice; 2 consecutive sections from the caudal slice) were prepared using a CryoStar NX70 cryostat (Epredia) at − 16 °C, in an RNase-free environment and mounted onto positively charged slides (Superfrost Plus, Fisherbrand #22-037-246). The sections were then stored at − 80 °C until use.

Spatial transcriptomics was performed using the 10 × Genomics Visium CytAssist platform (version 2) with human whole-transcriptome (WTA) probe chemistry (Visium V5 Slide—FFPE v2; Visium Human Transcriptome Probe Set v2.0, targeting 18,061 human genes), following the manufacturer's Visium CytAssist FFPE v2 protocol. For each rostro–caudal level, the two consecutive 10 µm sections were placed on the same Visium slide: the rostral pair (Upper Rostral, Lower Rostral) on slide V52L19-072 (positions A1 and B1), and the caudal pair (Upper Caudal, Lower Caudal) on slide V43L24-365 (positions A1 and D1).

snRNA-seq analysis of human LC

Raw gene–barcode matrices ("filtered_feature_bc_matrix") from two human LC sections (two Chromium reactions per section; LC001A–B, LC002A–B) were imported into R (v4.3.2) and processed with Seurat (v5.0.1) [83]. For each Chromium reaction, we generated a Seurat object, computed standard quality-control (QC) metrics: number of detected genes (nFeature_RNA), total UMI counts (nCount_RNA), and percentage of mitochondrial reads (percent.mt). The four Chromium reactions were then merged, yielding 2,347 nuclei before QC.

For initial processing, data were normalized, highly variable genes were selected, and expression values were scaled. Principal component analysis (PCA) was

performed on variable genes, and the four Chromium reactions were integrated using Seurat's reciprocal PCA (RPCA)–based layered integration workflow. A Uniform Manifold Approximation and Projection (UMAP) embedding was computed from the integrated reduction (40 dimensions), and a shared nearest-neighbor graph was built in the same space (FindNeighbors, 40 dimensions, k.param = 20). Unsupervised clustering was performed across a range of resolutions (0.1–1.5; FindClusters).

Broad cell types were annotated based on canonical marker expression. NE neurons were defined by *dopamine beta-hydroxylase* (*DBH*), *tyrosine hydroxylase (TH)* and *solute carrier family 6 member 2* (*SLC6A2)* together with pan-neuronal markers *stathmin 2* (*STMN2)* and *synaptotagmin 1* (*SYT1*). Additional neuronal clusters lacked *DBH*/*TH*/*SLC6A2,* but they expressed neuronal markers. Oligodendrocytes were identified by *myelin-associated glycoprotein (MAG), myelin basic protein (MBP), myelin oligodendrocyte glycoprotein (MOG), proteolipid protein 1 (PLP1)* and related genes; oligodendrocyte precursor cells (OPCs) by *platelet-derived growth factor receptor alpha (PDGFRA)* and *epidermal growth factor receptor (EGFR)*; astroependymal cells by *glial fibrillary acidic protein (GFAP)*, *gap junction protein alpha 1* (*GJA1)*, *aquaporin 4 (AQP4)*, *forkhead box J1 (FOXJ1)* and *coiled-coil domain containing protein 153 (CCDC153)*; microglia by *complement C1q B chain* (*C1QB)* and *allograft inflammatory factor 1 (AIF1)*. We also identified a low-quality cluster characterized by low gene counts and high mitochondrial percentages.

To remove low-quality nuclei, we implemented a data-driven, batch-aware QC strategy using custom R functions. QC batches were defined as sample × broad cell type (with small populations such as OPCs, astrocytes, and microglia grouped across sections). For each batch, kernel density estimates of log2-transformed nCount_RNA and nFeature_RNA were used to identify minima separating low-quality from high-quality nuclei, aided by Otsu-derived thresholds and, where applicable, Gaussian mixture modeling. Per-batch lower and upper thresholds for nCount_RNA and nFeature_RNA were then applied to the integrated object (Supplementary Table 1), and the low-quality cluster was explicitly removed. After QC, 2,071 of 2,347 nuclei (88.2%) were retained.

Cells passing QC were reprocessed using the same Seurat workflow: data were normalized, variable features were re-identified and scaled, sections were reintegrated using RPCA, and UMAP and graph-based clustering were recomputed. Final broad cell-type identities (NE neurons, other neurons and non-neuronal populations) were assigned based on UMAP visualizations and dot plots of canonical markers and were carried forward into downstream analyses.

snRNA-seq meta-analysis of human LC datasets

To place our LC dataset in a broader human context, we performed a meta-analysis integrating our snRNA-seq data with two published human pons datasets from Weber et al. [64] and Siletti et al. [66]. The Weber dataset comprised 20,191 neuronal and non-neuronal nuclei from the human LC region. For the Siletti dataset, six annotated pons sections were first screened for NE neurons by examining *DBH* expression across pontine nucleus (PN), afferent and efferent cranial nerve nuclei, pontine reticular formation (PnRF), parabrachial nuclei (PnRF–PB) and dorsal tegmental nucleus. A *DBH*-expressing neuronal cluster was detected in the PnRF–PB section, and only this section (24,155 neuronal and non-neuronal nuclei) was used for integration. These datasets were combined with the 2,071 QC-passed nuclei from our dataset, yielding a meta-dataset of 46,417 nuclei (Supplementary Table 2).

All meta-analysis steps were performed in R (v4.3.2) using Seurat (v5.0.1). Seurat objects from this study (Basak), Weber and Siletti were merged into a single object, with per-sample layers defined to enable multi-sample integration. Counts were normalized, highly variable genes were identified and data were scaled, followed by PCA.

Datasets were integrated using Seurat's multi-dataset integration framework. We used RPCA-based integration to generate a shared low-dimensional embedding, from which a UMAP representation was computed (30 dimensions). A shared nearest-neighbor graph was then constructed on this RPCA-integrated space (FindNeighbors, 30 dimensions, k.param = 20), and unsupervised clustering was performed over a range of resolutions, with resolution 0.6 selected for final annotations.

Cell types in the integrated meta-dataset were assigned by examining dot plots and feature plots of canonical markers, using the same marker sets as for the Basak dataset. NE neurons were identified by *DBH*, *TH* and *SLC6A2* expression; additional neuronal clusters expressed pan-neuronal markers (*STMN2*, *SYT1*) without *DBH*/*TH*/*SLC6A2*. Oligodendrocytes, OPCs, astrocytes, ependymal cells, microglia, and vascular cells were annotated based on established lineage markers. These integrated cell-type labels were used in subsequent meta-analyses.

Neuronal subtype analysis in the integrated snRNA-seq meta-dataset

To resolve neuronal diversity within the integrated LC meta-dataset, we first subset all nuclei annotated as neurons from the integrated object, yielding 33,375 neuronal nuclei across Basak, Weber, and Siletti. The RNA assay was retained, and per-sample layers were defined. We then applied Seurat's standard preprocessing and

integration workflow: counts were normalized, highly variable genes were identified, data were scaled and PCA was performed, followed by RPCA-based multi-sample integration to generate a neuron-specific integrated embedding. A UMAP was computed from this integrated space (30 dimensions), and a shared nearest-neighbor graph was constructed (FindNeighbors on 30 RPCA dimensions, k.param = 10). Graph-based clustering was performed over a range of resolutions, and a high-resolution setting (resolution 1.5) was selected for downstream neuronal subtype analyses, yielding 68 transcriptionally distinct neuronal clusters.

To functionally annotate neuronal subtypes, we focused on a curated list of G protein–coupled receptor and ligand genes derived from the IUPHAR Guide to Pharmacology (GtoP) database [84, 85]. Cluster markers were computed with Seurat's FindAllMarkers function restricted to this curated gene set, and cluster-enriched genes were defined based on effect size and specificity (for example, avg_log2FC > 0.5 with higher expression in the index cluster and low background expression in other clusters). For each cluster, the top two discriminative genes from this curated list were selected and visualized using dot plots to summarize neuropeptide and receptor signatures (Supplementary Fig. 1 d). Cluster labels were then derived by concatenating these two marker genes, with numeric suffixes applied only when the same gene pair occurred in more than one cluster. This strategy yielded three DBH$^+$ NE neuron subtypes: SLC6A2/DBH, DBH/SLC6A2, and SLC6A2/MET (MET proto-oncogene, receptor tyrosine kinase), which were used for downstream analyses.

Visium spatial transcriptomics analysis of human LC

For each Visium section, 10 × Genomics filtered feature–barcode matrices were imported into R (v4.3.2) using the Load10X_Spatial function in Seurat (v5.0.1). Standard spot-level QC metrics were computed, including total UMI counts (nCount_RNA), number of detected genes, and percentage of mitochondrial reads. To remove off-tissue or low-quality regions at the image periphery, we applied section-specific cropping based on Visium spot coordinates, visually matching areas with very low nCount_RNA to their positions in the coordinate space and excluding these spots by filtering on image row/column coordinates. Cropped objects from the four LC sections were then merged into a single Seurat object (12,495 spots in total).

Integration with published Weber LC Visium data and spatial cluster annotation

To place our spatial LC data in a broader context, we integrated our in-house Visium sections with published LC Visium data from Weber et al. [64] comprising 20,380 spots (Supplementary Table 3). Both datasets were merged into a single Seurat object (32,875 spots), with per-section layers defined. The combined LC Visium dataset was processed with SCTransform (default settings) and PCA, followed by Seurat's RPCA-based multi-sample integration on SCT-normalized data to generate a joint Visium embedding. A UMAP was computed from this integrated space (30 dimensions), and a shared nearest-neighbor graph was constructed (FindNeighbors on 30 integrated dimensions, k.param = 10). Clustering was performed over resolutions 0.1–1.5, and resolution 0.3 was selected to obtain a manageable number of spatial clusters for biological interpretation.

Because Visium spots do not correspond to single cells and can capture mixtures of neurons, glia, and vascular cells, we interpreted "neuronal" clusters as spots enriched for neuronal transcripts rather than purely single-cell neuronal profiles. Potential contributions from neighboring astrocytes, microglia, and other non-neuronal cell types should therefore be kept in mind when interpreting these annotations. Cluster annotation for the integrated Visium dataset was guided by canonical marker expression, including noradrenergic (*DBH*, *TH*, *SLC6A2*), pan-neuronal (*STMN2*, *SYT1*) and glial/vascular lineage markers (for example, *MAG*, *MOG*, *PLP1* for oligodendrocytes; *AQP4* for astrocytes; *FOXJ1*, *CCDC153*, *calcyphosine (CAPS)* for ependymal cells; *actin alpha 2 smooth muscle (ACTA2), transgelin (TAGLN)* for mural/vascular smooth muscle cells; *collagen type I alpha 1 chain (COL1A1)*, *collagen type III alpha 1 chain (COL3A1)*, *lumican (LUM), decorin (DCN)* for vascular leptomeningeal cell (VLMC)-like cells; and *hemoglobin subunit alpha 2* (*HBA2*), *hemoglobin subunit beta* (*HBB)* for erythrocytes), supplemented by a curated neurotransmitter/neuropeptide gene list. Based on these expression patterns, clusters were manually assigned to broad spatial cell classes: NE neurons, serotonergic neurons, *tachykinin precursor 1 (TAC1)*/*CRH* neurons, *adenylate cyclase activating polypeptide 1 (ADCYAP1)/VGF nerve growth factor inducible (VGF)* neurons, *proenkephalin (PENK)* neurons, *parvalbumin (PVALB)/sodium voltage-gated channel beta subunit 4 (SCN4B)* neurons, GABAergic neurons, glutamatergic neurons, oligodendrocytes, astrocytes, ependymal cells, vascular cells, and two unclassified clusters with no prominent marker signature (Supplementary Fig. 2c).

Animals

RNAscope in situ hybridization experiments were performed in 5-week-old male C57BL/6NTac mice. All mice were obtained from Taconic Biosciences. All animal care and experimental procedures followed the US National Institutes of Health Animal Care and Use guidelines and were approved by the Columbia University Animal Care

and Use Committee (IACUC). Animals were sacrificed according to Columbia University regulations using the appropriate protocol (#AC-AABF6552).

Housing and diets

Mice were housed at 22–24 °C constant temperature with a regular 12-h light/12-h dark cycle (lights were turned off at 7 pm), with no more than 5 adult animals per cage and ad libitum access to Purina 5058 chow diet and water.

Mouse brain dissection and tissue preparation

Mice were sacrificed via cervical dislocation followed by decapitation. Brains were immediately removed, frozen in dry ice, subsequently embedded in O.C.T. compound (Thermo Fisher Scientific, 23,730,571) and placed in dry ice to flash freeze. All brains were immediately stored at – 80 °C in an airtight container until further use.

For in situ hybridization, fresh-frozen brains were cut into 20 µm-thick serial coronal sections (resulting in 54–57 sections for the LC) using a CryoStar NX70 cryostat (Epredia) at – 16 °C, collected on Superfrost Plus microscope slides (3 sections per slide), dried at 20 °C for 1.5 h and stored at – 80 °C in an airtight container until use.

The first section was collected approximately at Bregma – 5.1 mm to Bregma – 6.1 mm, spanning the LC from rostral to caudal.

RNAscope HiPlex in situ hybridization

Given that snRNA-seq and Visium have limited sensitivity, we moved forward with the highly sensitive.

Table 1 Target genes for HiPlex RNAscope® Assay. (a) Channel setup for RNAScope HiPlex co-hybridization experiment. (b) Channel setup for RNAScope Multiplex Fluorescent v2 co-hybridization experiment

Gene	Channel	ISH Detection
Round 1		
Mc4r	C1-T1	488-Green
Dbh	C2-T2	550-Orange
Lepr	C3-T3	650-Red
Round 2		
Mrap2	C1-T4	488-Green
Pax7	C2-T5	550-Orange
Psen1	C3-T6	650-Red
Round 3		
Psen2	C1-T7	488-Green
Trem2	C2-T8	550-Orange
Crh	C3-T9	650-Red
Round 4		
App	C1-T10	488-Green
Sorl1	C2-T11	550-Orange
Apoe	C3-T12	650-Red

RNAscope technology. It allows for the detection of single RNA molecules and can more reliably assess lowly.

expressed genes which may escape detection in snRNA-seq or Visium.

One series, consisting of 57 fresh-frozen brain sections with a thickness of 20 µm, covering the entire mouse LC from rostral to caudal, was pre-treated and stained following the RNAscope HiPlex 12 Reagents Kit (488, 550, 650) (ACD # 324,108) user manual protocol (Advanced Cell Diagnostics (ACD) Document #324,419-USM). Briefly, sections were taken from – 80 °C and put directly in a 4% paraformaldehyde solution for 60 min, rinsed in PBS, and dehydrated in increasing ethanol concentrations. Sections were dried for 10 min followed by 30 min of Protease IV (ACD #322,336) treatment at room temperature to permeabilize the cells and subsequent washed with PBS. The pre-warmed probes mixture was added, and the probes were hybridized to the targeted genes at 40 °C for 2 h in a HybEZ II oven (ACD). The following probes were used: *Mc4r* (ACD #319,181-T1), *Dbh* (ACD #407,851-T2), *Lepr* (ACD #471,171-T3), *Mrap2* (ACD #1,067,291-T4), *paired box 7* (*Pax7*, ACD #314,181-T5), *Psen1* (ACD #451,011-T6), *Psen2* (ACD #450,981-T7), *Trem2* (ACD #1,082,891-T8), *corticotropin releasing hormone* (*Crh*, ACD #316,091-T9), *App* (ACD #578,001-T10), *Sorl1* (ACD #1,082,901-T11), *Apoe* (ACD #590,131-T12). The sections were washed in 1X wash buffer (ACD #310,091), and amplification reagents AMP1-AMP3 were incubated in succession at 40 °C with wash buffer steps in between. In the first imaging cycle, fluorophores T1–T3 were applied and hybridized with the tissue at 40 °C for 15 min. The sections were then washed in wash buffer, counterstained with DAPI solution for 30 s, and coverslips were directly mounted with ProLong Gold Antifade Mountant (Fisher Scientific #P36930). Slides were kept dark at 4 °C and images were captured in the following days. Fluorophores were then cleaved with freshly prepared 10% cleaving solution (stock, ACD #324,399) twice to ensure the fluorophores were removed entirely. This process was repeated for 3 more rounds to image fluorophores T4–T12. Sections were counterstained with DAPI every other round. Target genes and channels for each round are listed (Table 1a).

RNAscope multiplex fluorescent V2 assay

One series, consisting of 54 fresh-frozen brain sections with a thickness of 20 µm, covering the entire mouse LC from rostral to caudal, was pre-treated and stained according to the RNAscope Fluorescent Multiplex Reagents Kit (ACD #320,850) user manual protocol (ACD Document #320,293-USM). Briefly, sections were taken from – 80 °C and put directly in a pre-chilled 4% paraformaldehyde solution for 15 min at 4 °C and dehydrated in increasing concentrations of ethanol. Sections

were dried for 5 min and then incubated with Protease IV at room temperature for 30 min. The pre-warmed probes mixture was added, and the probes were hybridized to the targeted genes at 40 °C for 2 h in a HybEZ II oven. The following probes were used: *Mrap2* (ACD #1,067,291-C1), *Mc3r* (ACD #412,541-C2), *Mc5r* (ACD #478,381-C3), *Mc1r* (ACD #474,391-C2), and *Mc2r* (ACD #318,891-C3). Four consecutive rounds of amplifications (AMP1-AMP4) at 40 °C were followed by counterstaining with DAPI solution for 30 min and mounting of coverslips with ProLong Gold Antifade Mountant. Slides were kept dark at 4 °C and images were captured in the following days. Target genes and channels for each round are listed (Table 1b).

Digital image acquisition

Tiled z-stack images were acquired using the Zeiss LSM 710 laser scanning confocal microscope (Zeiss, Oberkochen, Germany). Images were obtained with 20X and 63X Zeiss Plan-Apochromat dry and oil objectives, respectively. All images were obtained in 1024 × 1024-pixel format. Zeiss ZEN software was used to gather the maximum intensity projection images.

For the sections processed using RNAscope HiPlex, 4 cycles of images were performed to image 12 RNA species, utilizing DAPI as reference in each round.

Image analysis

Images were analyzed using HALO (Indica Labs). For the sections processed using RNAscope HiPlex, the images from all rounds of staining were registered to each other to generate a 12 plex image using HALO software. In brief, a DAPI image from one of the rounds of imaging was used as the reference image. DAPI images from all other rounds of imaging were registered to this reference image, generating a transformation matrix of coordinate conversions that was applied to the remaining images from each imaging round to create one, unified coordinate system for all images from all rounds.

The HALO random forest classifier was trained for each section to identify the LC region by selecting two Dbh^+ regions within the LC and two Dbh^- regions outside the LC (Supplementary Fig. 4). For the analysis, cell segmenting and signal thresholds were independently established on each section using the software for all genes of interest. The number of RNA molecules per cell for each gene was detected for every cell within our annotation layer of each section. All analysis matrixes were exported to Microsoft Excel.

Matrices from each section were further analyzed to identify cells expressing each gene of interest as well as the average number of molecules per cell. Positive and negative thresholds for each gene of interest were established by selecting a region outside the Dbh-LC annotation layer and within the Dbh-LC annotation layer from the left and right sides of the LC from sections 34, 35, and 36 and calculating the minimum average number of molecules per cell and the maximum average number of molecules per cell in the selected regions (Supplementary Fig. 5a–c). Thresholds were manually set based on evaluation of the average minimum value. The following thresholds for positive cells were established: $Dbh^+ \geq 1$, $Lepr^+ \geq 2$, $Mc4r^+ \geq 2$, $Pax7^+ \geq 1$, $Psen1^+ \geq 3$, $Mrap2^+ \geq 2$, $Psen2^+ \geq 3$, $Trem2^+ \geq 3$, $Crh^+ \geq 4$, $App^+ \geq 7$, $Sorl1^+ \geq 2$, and $Apoe^+ \geq 4$. The following thresholds for negative cells were established: $Dbh^- = 0$, $Lepr^- \leq 1$, $Mc4r^- \leq 1$, $Pax7^- = 0$, $Psen1^- \leq 2$, $Mrap2^- \leq 1$, $Psen2^- \leq 2$, $Trem2^- \leq 2$, $Crh^- \leq 3$, $App^- \leq 6$, $Sorl1^- \leq 1$, and $Apoe^- \leq 3$ (Supplementary Fig. 5 d).

Statistical analysis

Statistical analysis was performed using GraphPad Prism 10.0.0. Comparisons between two normally distributed groups were performed by simple two-tailed unpaired student's *t*-test. All *p* (alpha) values < 0.05 were considered statistically significant.

Results

Single-nucleus transcriptomics and meta-analysis of the human LC

We first performed snRNA-seq on two anatomically defined human LC sections using the 10 × Genomics Chromium platform (Fig. 1a). After data-driven, batch-aware QC (Supplementary Table 1), 2,347 nuclei were retained for downstream analysis. UMAP visualization of this dataset revealed six major classes comprising 463 NE neurons, 897 other neurons, 493 oligodendrocytes, 56 OPCs, 131 astroependymal cells and 31 microglia (Fig. 1b).

To place this dataset in a broader human context, we next integrated our (Basak) LC nuclei with two recently published snRNA-seq datasets from the human pons: the Weber et al. dataset [64], centered on the LC region, and the Siletti et al. dataset [66] containing a parabrachial nuclei section that includes DBH^+ NE neurons. The resulting meta-dataset comprised 46,417 nuclei (Supplementary Table 2). After Seurat RPCA-based integration, cells from all three studies were extensively intermingled in the UMAP space, indicating effective batch correction (Supplementary Fig. 1a). Within this integrated embedding, major cell classes again segregated into coherent clusters, and all three datasets contributed to each lineage, including NE neurons (346 Basak, 306 Weber and 113 Siletti), other neurons (1,012; 16,201; 15,397), oligodendrocytes (491; 1,842; 4,945), OPCs (56; 288; 1,168), astrocytes (122; 400; 1,510), ependymal cells (2; 380; 5), microglia (36; 277; 763) and vascular cells (6; 497; 254) (Fig. 1c). QC metrics—total UMI counts, number

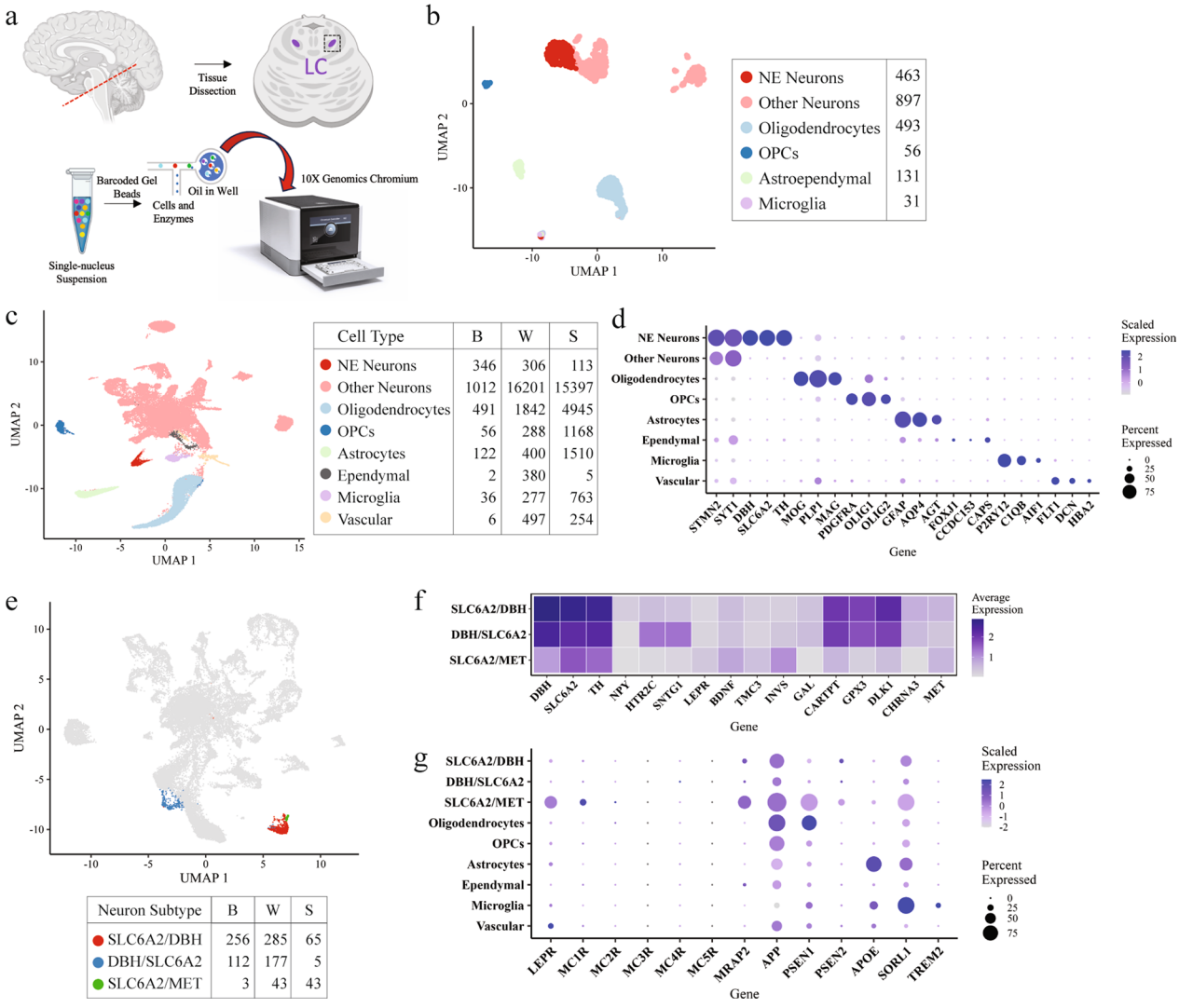

Fig. 1 Single-nucleus transcriptomics of the human LC **a** Schematic of the experimental workflow for snRNA-seq from the human LC region, including tissue dissection, single-nucleus suspension preparation, and processing with the 10×Genomics Chromium platform. **b** UMAP representation of nuclei from this study colored by broad cell-type annotation, revealing NE neurons, other neurons, oligodendrocytes, oligodendrocyte precursor cells (OPCs), astroependymal cells and microglia. The accompanying table summarizes cell numbers per class. **c** UMAP of the integrated snRNA-seq meta-analysis combining Basak (this study; B), Weber (W) and Siletti (S) datasets, colored by cell type. The table lists cell numbers for each major class across studies, demonstrating robust cross-dataset integration. **d** Dot plot of canonical marker genes supporting the cell-type assignments in c (for example, *DBH/SLC6A2* in NE neurons, *MOG/PLP1* in oligodendrocytes). **e** Neuronal nuclei from c were subsetted and reintegrated. DBH$^+$ NE neuron subtypes (SLC6A2/DBH, DBH/SLC6A2 and SLC6A2/MET) are highlighted on the UMAP, and their abundances per dataset are summarized in the table. **f** Heatmap showing average expression of key NE neuron markers and additional literature-curated and differentially expressed genes across the three DBH$^+$ subtypes, illustrating shared core NE identity and subtype-specific transcriptional signatures. **g** Dot plot depicting expression of melanocortin pathway components and AD–related genes across NE neuron subtypes and major non-neuronal cell classes

of detected genes and mitochondrial RNA fraction—showed largely overlapping distributions across Basak, Weber, and Siletti within each major class, with higher mitochondrial read fractions in neurons of Basak and NE neurons from Weber, and higher detected genes and UMI counts in neuronal clusters from Siletti (Supplementary Fig. 1b).

We then focused on neuronal diversity within this integrated LC meta-dataset. Subsetting all nuclei annotated as neurons yielded 33,375 neuronal nuclei, which were reintegrated and reclustered, resulting in 68 transcriptionally distinct neuronal subtypes (Supplementary Fig. 1c). To functionally annotate these subtypes, we restricted cluster-marker discovery to a curated list of GPCRs and ligands [84, 85]. Each cluster was labeled by a discriminative gene pair that captured its neuromodulatory identity (Supplementary Fig. 1 d).

Within the integrated neuron dataset, three DBH$^+$ NE neuron subtypes were resolved and designated by their defining gene pairs: SLC6A2/DBH, DBH/SLC6A2 and

SLC6A2/MET (Fig. 1e). These subtypes were present in all three datasets, although with differing abundances: for SLC6A2/DBH we observed 256 Basak, 285 Weber and 65 Siletti nuclei; for DBH/SLC6A2, 112, 177 and 5 nuclei; and for SLC6A2/MET, 3, 43 and 43 nuclei, respectively (Fig. 1e). A heatmap of average expression confirmed that all three subtypes shared a core noradrenergic transcriptional program with high levels of *DBH*, *SLC6A2* and *TH*, but differed in a set of additional genes curated from the literature, including *neuropeptide Y* (*NPY*), *GAL*, *glutathione peroxidase 3 (GPX3)*, *delta like non-canonical Notch ligand 1 (DLK1)* and *cholinergic receptor nicotinic alpha 3 subunit (CHRNA3)* [22, 86, 87], as well as from differential expression analyses (Fig. 1f). For instance, *NPY* expression was particularly enriched in the DBH/SLC6A2 subtype, whereas *5-hydroxytryptamine receptor 2C (HTR2C)* and *syntrophin gamma 1 (SNTG1)* were relatively higher in DBH/SLC6A2. *LEPR*, *brain derived neurotrophic factor (BDNF)*, *transmembrane channel like 3 (TMC3)* and *inversin (INVS)* were higher in SLC6A2/MET. *GAL*, *CART prepropeptide (CARTPT)*, *GPX3*, *DLK1* and *CHRNA3* showed subtype-biased expression across SLC6A2/DBH and DBH/SLC6A2. Together, these signatures indicate that human LC NE neurons comprise transcriptionally specialized populations beyond a shared catecholaminergic core.

Finally, we examined the distribution of melanocortin pathway components and AD-related genes across neuron subtypes and major non-neuronal classes (Fig. 1g, Supplementary Fig. 1e). *LEPR* expression was concentrated in the SLC6A2/MET subtype, with additional signal in other neuronal subtypes and in vascular cells. *MC1R* was mainly detected in the SLC6A2/MET subtype, whereas *MC2R*, *MC3R*, *MC4R*, and *MC5R* transcripts were generally rare and sparsely detected. *MRAP2*, a key melanocortin receptor accessory protein, was enriched in SLC6A2/MET and SLC6A2/DBH subtypes, as well as in additional neuronal subtypes and ependymal cells. AD-associated genes displayed broader patterns: *APP* and *PSEN1* were widely expressed across neuronal and non-neuronal populations, with *PSEN1* showing relative enrichment in the SLC6A2/MET subtype; *PSEN2* was expressed predominantly in neuronal populations; *APOE* was strongly expressed in astrocytes with additional signal in microglia, vascular cells, and some neuronal subtypes, but was essentially absent from NE neurons; *SORL1* was prominent in microglia with additional expression in astroependymal cells and neuronal subtypes including NE populations; and *TREM2* expression was essentially restricted to microglia. Together, these snRNA-seq analyses define the cellular architecture of the human LC and its surrounding region and highlight transcriptionally specialized NE neuron subtypes with differential engagement of melanocortin and AD-related pathways.

Visium spatial transcriptomics of the human LC

The 10 × Genomics Visium Spatial Gene Expression platform was used to map the LC transcriptome in its morphological context. The anatomic right LC of a neurotypical donor was sampled in two blocks, one rostral and one caudal (Fig. 2a). Two adjacent 10 µm sections from the rostral block (Upper Rostral, Lower Rostral) and two adjacent 10 µm sections from the caudal block (Upper Caudal, Lower Caudal) were processed for Visium, providing coverage along the rostral–caudal axis of the LC (Fig. 2a). After image-based cropping of low-UMI peripheral regions, 12,495 spots were retained across the four sections.

To place these spatial data in a broader context, we integrated our LC Visium sections with published LC Visium data from Weber et al. [64], which contributed 22,853 spots from four additional donors, resulting in 35,348 spots in total (Supplementary Table 3). Integrated UMAP embedding of Basak and Weber spots showed contribution of both datasets to most clusters, indicating successful cross-study integration (Supplementary Fig. 2a). Clustering followed by marker-based annotation resolved spatial domains enriched for NE neurons, serotonergic neurons, TAC1/CRH neurons, ADCYAP1/VGF neurons, PENK neurons, PVALB/SCN4B neurons, GABAergic neurons, glutamatergic neurons, oligodendrocytes, astrocytes, ependymal cells, vascular cells and two unclassified spot populations (Supplementary Fig. 2b). Because each spot captures transcripts from multiple cells, these categories represent cell type–enriched spots rather than single-cell identities. A dot plot of canonical markers supported these annotations, and violin plots summarizing quality-control metrics (sum UMI counts, number of detected genes and mitochondrial RNA percentage) are provided in Supplementary Fig. 2c, d. Projection of these annotations back onto individual sections revealed a stereotyped LC architecture in both Basak and Weber donors, with a compact NE-enriched band surrounded by additional neuronal and glial territories (Fig. 2b, Supplementary Fig. 3a).

We next examined spatial gene-expression patterns for noradrenergic, melanocortin and AD-associated transcripts within the Visium LC sections. In the representative Lower Rostral section from our donor, *DBH* expression sharply delineated the LC NE neuron core (Fig. 2c). *MRAP2* and *PSEN2* were detectable in a subset of NE-enriched spots and in surrounding neuron-enriched domains, whereas *APP* and *APOE* showed a broad distribution across the tissue (Fig. 2c). *PSEN1*, *SORL1* and *TREM2* were expressed at lower levels, with signal scattered throughout the section (Fig. 2c).

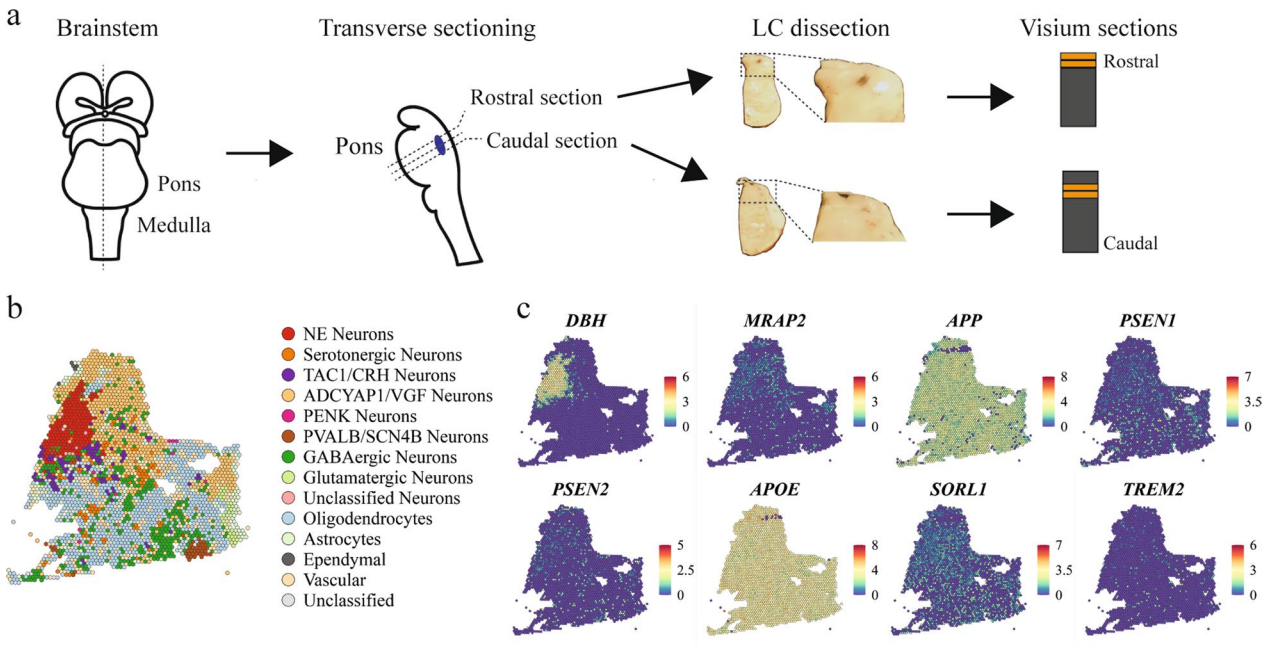

Fig. 2 Visium spatial transcriptomics of the human LC. **a** Schematic of workflow from separation of the hemi brainstem through sagittal cut to transverse sectioning of the metencephalon (LC shown in blue), followed by dissection of the LC (the boxed portion of the slices enlarged on the right side embedded in O.C.T. compound) and subsequent generation of consecutive sections for Visium spatial transcriptomics (10 micron sections, shown in orange). Photographs and sections were taken from the blocks' rostral face. **b** Spatial organization of cell types in a representative Visium LC section (Lower Rostral), revealing distinct NE, other neuronal and glial populations. Each Visium spot captures transcripts from multiple cells; cell-type labels therefore indicate spots enriched for a given cell class rather than single-cell identities. **c** Spatial gene expression maps for selected noradrenergic markers, melanocortin pathway and AD–related genes in the same Visium section, illustrating their distribution and relative expression levels

Examination of all sections across Basak and Weber donors revealed similar patterns for these genes (Supplementary Fig. 3b). Consistent with the noradrenergic identity of this domain, *SLC6A2* closely paralleled *DBH* in outlining the LC band, while *MC1R* and *MC4R* were detected only in a small subset of LC spots, as well as in neuron-enriched regions adjacent to the LC. *LEPR*, *MC2R*, *MC3R*, and *MC5R* were expressed only very sparsely or were not detectably expressed (Supplementary Fig. 3b).

Together, these Visium analyses demonstrate that the human LC forms a conserved noradrenergic domain across individuals, defined by spatially restricted *DBH* and *SLC6A2* expression, and that *MRAP2* is detectable within this LC territory. AD-associated genes such as *APP*, *PSEN1*, *PSEN2*, *APOE*, *SORL1*, and *TREM2* display broader spatial patterns, consistent with their expression in multiple neuronal and non-neuronal populations. These observations are largely in line with the cell type–resolved expression profiles obtained from our snRNA-seq analysis.

Melanocortin and AD-associated gene expression profiling across the entire mouse LC using RNAscope HiPlex

The human spatial transcriptomic data of the LC indicate heterogeneity of gene expression within the NE neurons (identified by *DBH*). We further assessed the heterogeneity with regards to genes of the melanocortin pathway and those associated with AD using RNAscope HiPlex. The complete mouse LC was included in 57 coronal sections (Fig. 3a). Each section was stained with twelve distinct probes, imaged using a confocal microscope, and then images were overlayed upon each other to generate a HiPlex image (Fig. 3b; Table 1). The images of the LC obtained were compared to reference images from the mouse Allen Brain Atlas using *Dbh* as the genetic marker for NE neurons within the region. Dbh^{+} cells were used to delineate the LC (Fig. 3c).

In Fig. 4, a representative overview of each transcript's image is displayed from section 35, one of the sections which falls within the central region along the rostral-caudal axis. Here Dbh^{+} LC cells are highly abundant (Fig. 4a-l). All genes of interest present in our 12 channels were overlayed upon each other to generate a HiPlex image of each LC section (Fig. 4m). The random forest classifier was trained to identify the LC by selecting two Dbh^{+} regions within the LC and two Dbh^{-} regions outside the LC (Supplementary Fig. 4 a, b). An example of an input used to outline an LC region within a section is provided (Supplementary Fig. 4c). Across the sections, the number of *Dbh*-expressing cells increased from rostral to caudal, with higher numbers beginning at section 22, the maximum in sections 35–39, and remaining high up to section 57. None of the other transcripts

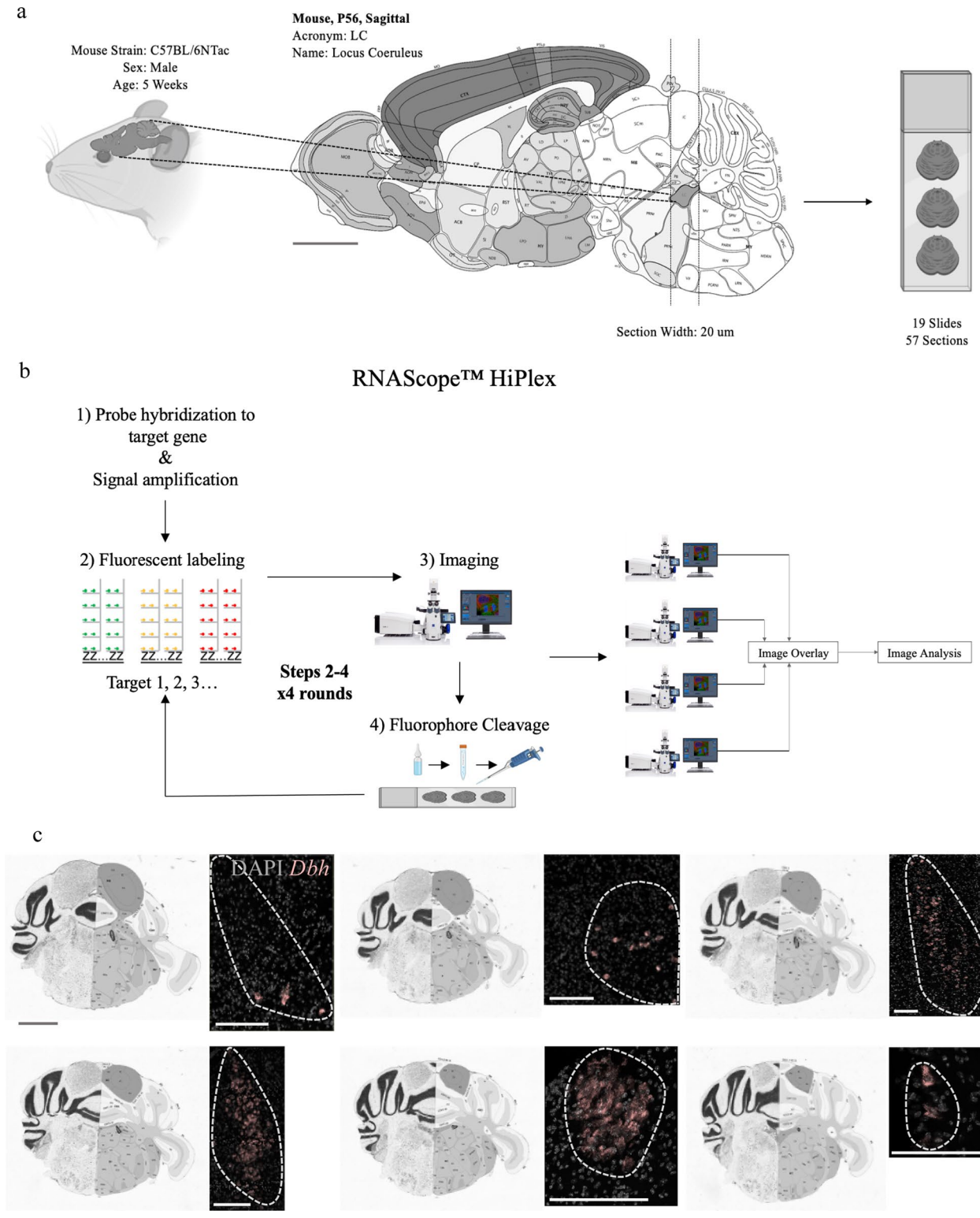

Fig. 3 (See legend on next page.)

examined in this experiment followed the *Dbh* gene distribution. While each gene presented with a distinct dynamic, within sections 25–28 and 34–39, all of them had one peak. However, there was no single section in which all genes peaked (Fig. 4n).

We quantified the expression of each of the melanocortin pathway genes and each of the AD-related genes in

(See figure on previous page.)

Fig. 3 RNAScope HiPlex workflow and LC detection. **a** Fresh, frozen adult mouse brain tissue was obtained and sectioned, resulting in 57 sections of 20 µm each for the LC, extending from rostral to caudal, with 3 sections per slide. Brain Image adapted from Allen Brain Atlas. Scale Bar = 1860 µm. Image generated using Biorender (https://biorender.com/). **b** The RNAScope HiPlex assay was performed by hybridizing the gene-specific mRNA probes to our sample. Then one round of amplification and fluorophore application for 3 probes was completed, which was subsequently followed by imaging of all slides. The applied fluorophores were then cleaved and the process was repeated for a total of four rounds. The images from each round were overlayed and analysis was completed using Halo software. Image generated using Biorender (https://biorender.com/). **c** Sections from rostral (upper left corner) to caudal (bottom right corner). Cells were counterstained with DAPI (gray). *Dbh*$^+$ cells were used as a marker for the LC. Six representative LC sections from the HiPlex experiment were matched to the six LC sections from the Allen Brain Atlas. Allen Brain (Right): Scale Bar = 1675 µm. *Dbh*$^+$-LC (Left): Scale Bar = 200 µm

Dbh$^+$ or *Dbh*$^-$ cells relative to the total number of *Dbh*$^+$ or *Dbh*$^-$ cells. We also quantified the average number of RNA foci per cell in the two categories, *Dbh*$^+$ or *Dbh*$^-$, within the LC (Fig. 5; Supplementary Fig. 5). Representative images for each gene of interest were selected from sections 31 to 35 (Table 2). *Mrap2* is expressed in 71.8% of *Dbh*$^+$ and 19.7% of *Dbh*$^-$ cells. However, the number of *Mrap2* molecules per cell are much greater in the *Dbh*$^+$ compared to the *Dbh*$^-$ cells (Fig. 5a). Less than 5% of both *Dbh*$^+$ and *Dbh*$^-$ cells express *Lepr* or *Mc4r* (Fig. 5b, c). AD-related genes are expressed at different levels in the *Dbh*$^+$ and *Dbh*$^-$cells of the LC (Fig. 5d–k; Table 3a, b).

Co-expression of melanocortin receptor family genes with Mrap2

Mrap2 interacts with all of the melanocortin receptor proteins, Mc1r-Mc5r [88]. One of this study's goals is to identify which melanocortin receptors are co-expressed with *Mrap2* in the LC. By HiPlex, *Mc4r* expression is very limited in the LC; necessarily the number of cells in which both *Mc4r* and *Mrap2* transcripts could be detected. Less than 3% of *Mrap2* positive cells co-express *Mc4r* (Table 4). We looked for other melanocortin receptors that might be co-expressed with *Mrap2.* In an RNAscope Multiplex experiment, limited co-expression *of Mrap2* with *Mc1r* (< 1%) or *Mc3r* (< 5%), and higher co-expression of *Mrap2* with *Mc2r* (10.9%) or *Mc5r* (17.9%) was detected within LC cells (Fig. 6a–d; Table 4). Overall, a higher percentage of cells co-expressed *Mrap2* and *Mc5r* compared to the other melanocortin receptor genes.

Identification of LC cellular population co-expressing Mrap2 and AD-related genes

Finally, after identifying the abundant expression of *Mrap2* in the LC, we analyzed the RNAscope HiPlex data further to see if there is a population of cells which co-expresses *Mrap2* and the AD-related genes. We identified cells which co-express *Mrap2* and familial AD-genes-*App, Psen1, and Psen2-* along with *Dbh* (Fig. 7a). 40.1% of *App*$^+$, 49.3% of *Psen1*$^+$, and 35.9% *Psen2*$^+$ cells also expressed *Mrap2* and *Dbh;* 21.4% of all cells in the LC co-expressed *App, Psen1, Psen2, Mrap2,* and *Dbh* (Fig. 7c, e). There were fewer cells co-expressing *Mrap2, Dbh*, and GWAS AD genes-*Trem2, Sorl1, Apoe* (Fig. 7b). 16.3% of *Trem2*$^+$, 50.1% of *Sorl1*$^+$, and 21.6% *Apoe*$^+$ cells also expressed *Mrap2* and *Dbh* and 4.6% of all cells in the LC co-expressed *Trem2, Sorl1, Apoe*, *Mrap2*, and *Dbh* (Fig. 7d, f; Table 3c). There were no cellular populations identified which co-expressed *Mrap2*, *Dbh*, and all AD-related genes (Fig. 7g; Table 3c).

Discussion

Numerous studies have described obesity as a risk factor for AD. The leptin-melanocortin pathway is a key mediator of food intake and energy expenditure and may be involved in the pathophysiology of this association [1, 62, 89–91]. Impaired leptin signaling may play a role in AD pathogenesis [19, 20, 92, 93]. We investigated whether the melanocortin genes are expressed in the LC—one of the brain regions known to be affected in the earliest stages of AD.

In the meta-analysis of snRNA-seq datasets from the human LC region, we identified three transcriptionally specialized DBH$^+$ NE neuron subtypes and mapped melanocortin and AD-associated genes to this data. *MRAP2* emerged as the most prominent melanocortin-related transcript in NE neurons, being enriched in SLC6A2/MET and SLC6A2/DBH subtypes. In contrast, melanocortin receptors themselves were expressed at low levels: *MC1R* was mainly detected in the SLC6A2/MET subtype, while *MC2R*, *MC3R, MC4R*, and *MC5R* transcripts were generally rare and sparsely detected. AD-associated genes showed broader, cell type–specific patterns that were consistent with their known biology. Together, these snRNA-seq data reveal a transcriptionally heterogeneous NE neuron population in the human LC with differential engagement of melanocortin and AD-related pathways.

Visium Spatial Transcriptomics identified distinct spatial arrangements of cellular populations in the human LC region. Our primary focus were the LC NE neurons, with the biosynthetic enzyme *DBH* serving as a marker for NE-producing neurons [94]. Integration of all Visium sections from our donor with published LC Visium data from Weber et al. [64] demonstrated a conserved noradrenergic LC domain and surrounding peptidergic, GABAergic, glutamatergic, and glial territories. Consistent with the snRNA-seq results, *MRAP2* expression was detectable within the LC territory. By contrast, melanocortin receptors were at or near the detection limit of the

Visium platform: *MC1R* and *MC4R* were observed only in a small subset of NE-enriched spots and adjacent neuron-enriched regions, whereas *LEPR*, *MC2R*, *MC3R*, and *MC5R* were very sparsely or not detectably expressed. As previously established, *APP* showed widespread expression across LC and non-LC tissue. *PSEN1* and *SORL1* were expressed at lower levels and were scattered throughout neuronal and glial regions, whereas *PSEN2* was detectable in neuronal territories. *TREM2* signal was sparse. In summary, our Visium analysis corroborates the presence of a conserved noradrenergic core in the human LC, confirms *MRAP2* expression within this domain, and shows that AD-associated genes exhibit broader spatial patterns, consistent with their distribution across multiple neuronal and non-neuronal cell types observed in our snRNA-seq meta-analysis.

With the highly sensitive RNAscope technology, we were able to detect all probed genes of interest. There was considerable heterogeneity of all gene expression profiles analyzed within the LC. Each of the melanocortin pathway and AD-associated genes showed a distinct gene expression pattern within Dbh^{+} neurons across the mouse LC. These findings are in agreement with our Visium study in the human LC and confirm prior studies on the heterogeneous molecular signatures of the Dbh^{+} neurons within the LC [12, 86, 95–99].

Each gene had its own unique expression pattern within Dbh^{+} and Dbh^{-} cells of the LC. There was limited expression of *Lepr* within the mouse LC. This is in agreement with a previous snRNA-seq study of the LC that identified *Lepr* in addition to strong *Galanin (Gal)* expression in NE neurons [63]. The functional significance of this small population of *Lepr*-expressing cells is unknown. In other brain regions it has been shown that Gal can act as an important mediator of leptin action [100]. Among the melanocortin pathway genes, *Mrap2*-expressing cells were by far the most abundant within the LC. Mutations in *MRAP2* have been associated with obesity [101–103]. MRAP2 interacts with all 5 melanocortin receptors, MC1R, MC2R, MC3R, MC4R, and MC5R, to regulate cell surface expression and signaling via response to α-MSH [88, 101, 103–107].

Of the melanocortin receptors co-expressed in $Mrap2^{+}$ cells, *Mc5r* was highest, followed by *Mc2r*. Although MC2R and MC5R are classically associated with peripheral functions, there is evidence for the central effects of both receptors in stress, immune, and metabolic processes, which is relevant for our study of LC-NE neurons and AD pathology [12, 14, 51–55]. MC2R, the canonical ACTH receptor, is a key mediator of hypothalamic–pituitary–adrenal (HPA) axis signaling. Central ACTH–melanocortin signaling has been shown to modulate arousal, stress responsiveness, and noradrenergic activity, which are all core functions of LC NE neurons [12, 51, 56]. Chronic stress and dysregulated HPA axis activity are well-established contributors to LC degeneration and AD pathology, providing a mechanistic context for MC2R expression in these neurons [50, 52, 57, 58]. MC5R, which plays roles in both exocrine and immune regulation, has also been implicated in central anti-inflammatory and neuroprotective melanocortin signaling [12, 53, 55]. Neuroinflammation is a critical driver of LC vulnerability and early tau pathology in AD. Melanocortin receptors, including MC5R, have been shown to suppress pro-inflammatory signaling and oxidative stress in neural tissues [52, 53, 55, 59–63]. Within the context of our study, the identification of *MC2R* and *MC5R* expression in LC NE neurons expands the canonical view of melanocortin signaling beyond hypothalamic feeding circuits and supports a broader framework in which melanocortin pathways intersect with stress, immune regulation, and neurodegeneration.

Despite the reported findings, many *Mrap2*-expressing cells do not co-express melanocortin receptor genes (Supplementary Fig. 6). MRAP2 is considered a broad-spectrum GPCR modulator [108], and many GPCRs are expressed in the LC [63, 109]. This raises the question of which other GPCRs are co-expressed with *MRAP2* in cells lacking melanocortin receptors. To address this, we systematically examined the broader GPCR landscape using a curated IUPHAR GPCR gene list [84, 85], generating dot plots across NE neuron and other neuronal subtypes and major non-neuronal classes in the integrated snRNA-seq meta-dataset, as well as corresponding spatial maps in the integrated Visium dataset (Supplementary Figs. 7 and 8). These analyses confirm that numerous additional GPCRs are expressed in the human LC/pons, including receptors involved in energy homeostasis that are known to interact functionally with *MRAP2*, such as orexin receptor (*OXR1* [*HCRTR1*]) and *MCHR1* [95–98]. The expression of these receptors has been also previously reported in the LC [39, 94, 99–102] and, together with our GPCR-wide profiling, highlights a broader set of candidate *MRAP2* interaction partners beyond the melanocortin receptors.

Among the AD-associated genes, *App* and *Apoe* were highly expressed within the LC. *Apoe* expression was higher in non-neuronal cells. Consistent with our findings, *Apoe* is primarily expressed in astrocytes, but is also present in CNS neurons. *Apoe* is synthesized by astrocytes, however, neuronal expression and synthesis of *Apoe* increases with excitotoxic stress [110]. *APP* is expressed in neurons, astrocytes, microglia, oligodendrocytes, and endothelial cells [67, 73], we confirmed this distribution. Mutations in APP and presenilins contribute to increased amyloid-beta accumulation and AD pathogenesis [68–70, 73]. *APP*, *PSEN1*, and *PSEN2* mutant genes are familial and strong contributors to early

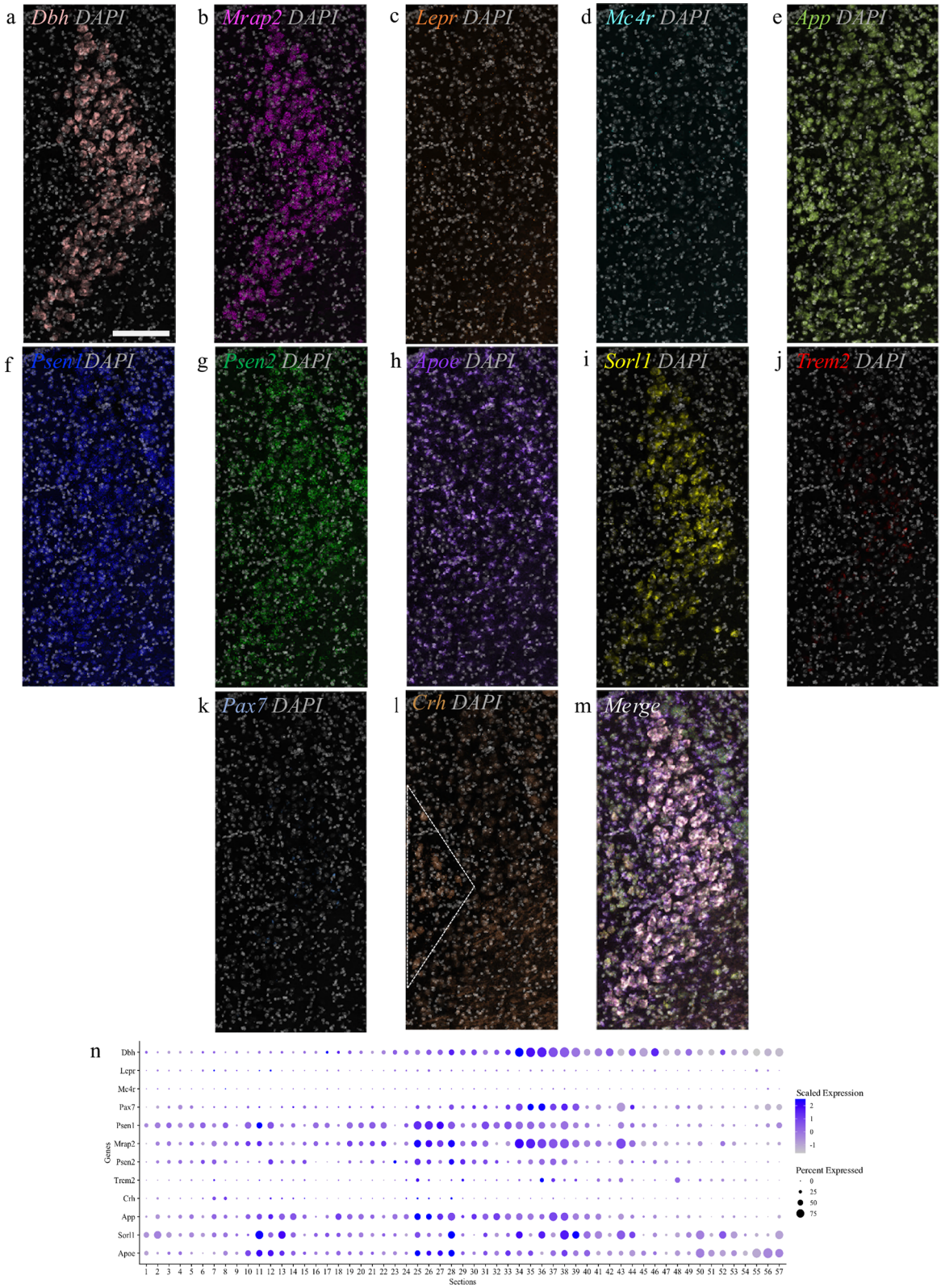

Fig. 4 HiPlex RNAScope detection of AD-associated and leptin-melanocortin genes in the LC. **a**–**m** Cells were counterstained with DAPI (gray). Genes of interest were detected with fluorescent labeled probes and imaged in four rounds. Images displayed are from section 35 of the LC. Merged image shown in panel "m". Magnification × 63. Scale Bar = 200 µm. **n** Dot plot graph showing expression levels of signature genes across each LC section. The size of the dot indicates the proportion of cells expressing each gene of interest. The spectrum of colors indicates the mean expression level. Section 1 is the most rostral section and section 57 is the most caudal section

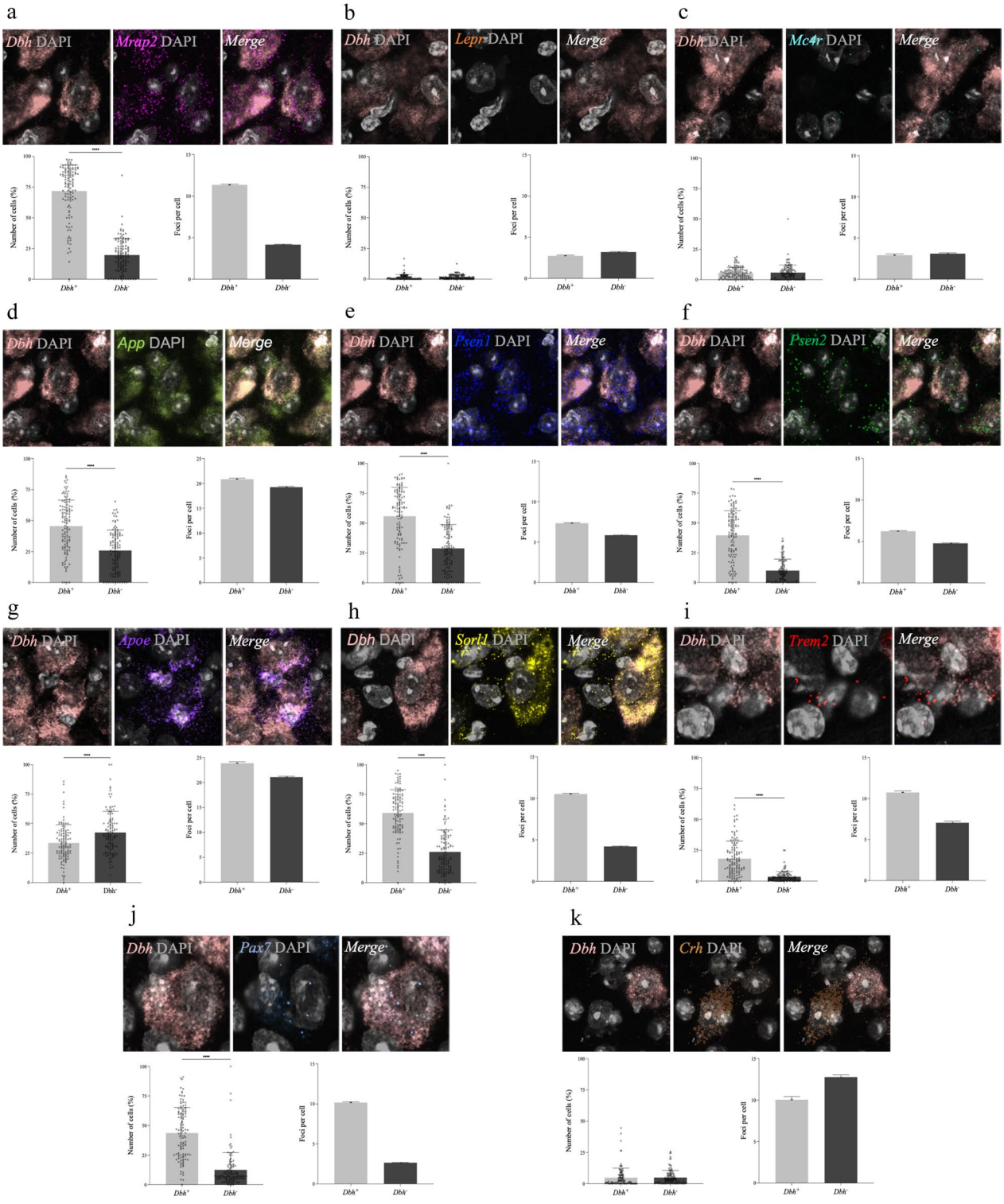

Fig. 5 HiPlex RNAScope co-expression of genes of interest in *Dbh*$^{+}$and *Dbh.*$^{-}$ LC cells. **a**–**k** Top panel: cells were counterstained with DAPI (gray). Genes of interest were detected with fluorescent labeled probes and imaged in four rounds. Magnification × 63. Scale Bar = 10 µm. Bottom panel: bar graphs represent quantification of double-positive cells expressed as a percentage with individual data points for each section value (Data are means +/− SD) and the average number of molecules per cell (Data are means +/− SEM). Two-tailed unpaired student's *t*-test, ****$p < 0.0001$

Table 2 Representative sections for selected genes of interest. Representative images displayed in Fig. 5 were selected from sections 31 and 35. The genes represented from each section are listed

Section number	Gene
31	*Mrap2*
	Mc4r
	App
	Psen1
	Psen2
	Apoe
	Trem2
35	*Lepr*
	Sorl1
	Pax7
	Crh

Table 4 Percentage of each melanocortin receptor *Mc1r–Mc5r* co-expressing *Mrap2*. Mean percentage of co-expression from all sections from each experiment

	***Mrap2*$^+$**
Mc1r	0.8%
Mc2r	10.9%
Mc3r	4.2%
Mc4r	2.3%
Mc5r	17.9%

AD pathogenesis [71, 72]. Our study is agreement with prior work showing *Psen1* expression in neurons, astrocytes, oligodendrocytes, microglia, and endothelial cells [67]. Consistent with the literature, we find *PSEN2* is primarily expressed in neurons [111]. Cells co-expressing these familial AD genes were identified in the LC. Of note, APP and PSEN1 are not differentially regulated with respect to transcript level in LC neurons in the brains of individuals with mild/moderate AD relative to the brains of individuals with no cognitive impairment or mild cognitive impairment [112].

The expression of other AD-associated genes was also investigated. *SORL1* is now considered to be a causal AD gene [77]. Sorl1 regulates the trafficking and processing of App and interacts with tau and Apoe as an Apoe receptor. *Sorl1* is widely expressed in the brain, predominantly in hippocampal neurons, brainstem nuclei and Purkinje cells [75, 76]. Decreased SORL1 is associated with increased beta-amyloid accumulation. [75, 76]. Our study identified cellular populations expressing *Sorl1* in both neuronal and non-neuronal populations of the LC. Other AD-related genes including *App*, *Apoe*, *Psen1*, and *Psen2* were expressed in some of these cells. *Trem2* is expressed in the LC, although at lower levels than the other AD-related genes. Whole exome sequencing and GWAS have identified *Trem2* alleles that are associated with increased risk of developing AD [80, 81, 113]. Lack of Trem2 is believed to result in impaired recruitment of microglia leading to plaque formation, amyloid beta damage to neuronal cells, and neuroinflammation [82, 114, 115]. *Trem2* is expressed throughout the brain including the hippocampus, brainstem, and cerebellum [79]. Literature predominantly suggests that *Trem2* is expressed exclusively in microglia; however there have been reports of *Trem2* expression in neurons, astrocytes, and oligodendrocytes [114–125].

Pax7 and *Crh* are expressed in the LC. There are *Pax7*$^+$ and *Pax7*$^-$cellular populations within the LC. The projections to the rest of the brain as well as function are thought to differ [96]. In our study, *Pax7* expression was more abundant in specific regions of the LC. *Crh* expression within the LC was sparse, however, there was a dense population of *Crh* neurons detected adjacent to the LC. *Crh* expression has been detected in Barrington's nucleus, which is adjacent to the LC [63, 126].

A high percentage of *Mrap2* expressing cells within the LC are co-expressed with familial AD genes. This co-expression is a predicate for co-regulation of these receptors and has relevance for assessment of any functional links between the melanocortin and AD pathways to further the understanding of the conjunction of obesity and AD. LC NE neurons regulate neuroinflammation. NE has an anti-inflammatory effect on microglia

Table 3 Selected values from Figs. 5 and 7

a		*App*	*Psen1*	*Psen2*	*Apoe*	*Sorl1*	*Trem2*	*Pax7*	*Crh*
	Dbh$^+$	45.5%	55.7%	39.6%	33.6%	59.2%	18.3%	43.7%	4.8%
	Dbh$^-$	25.9%	28.9%	10.0%	42.4%	26.0%	3.6%	12.5%	4.9%
b		*App*	*Psen1*	*Psen2*	*Apoe*	*Sorl1*	*Trem2*	*Pax7*	*Crh*
	Dbh$^+$	20	7	6	23	10	10	10	10
	Dbh –	19	5	4	21	4	7	2	12
c		Familial AD genes	GWAS AD genes	All AD-related genes					
	Mrap2$^+$	21.4%	4.6%	0.03%					
	Mrap2$^-$	0.42%	0.35%	0.03%					

(a) Percentage of total Dbh$^+$ cells co-expressing Dbh and each selected gene of interest or percentage of total Dbh$^-$ cells expressing each selected gene of interest. Percentage is mean value of all sections. (b) Foci per cell for each selected gene of interest in *Dbh*$^+$ or *Dbh*$^-$ cells. Value is the mean value of all sections. (c) Percentage of total *Dbh*$^+$ cells co-expressing *Dbh* and familial AD genes (*App*, *Psen1*, *Psen2*), GWAS AD genes (*Sorl1*, *Trem2*, *Apoe*), or all AD genes (*App*, *Psen1*, *Psen2*, *Sorl1*, *Trem2*, *Apoe*). Percentage is mean value of all sections

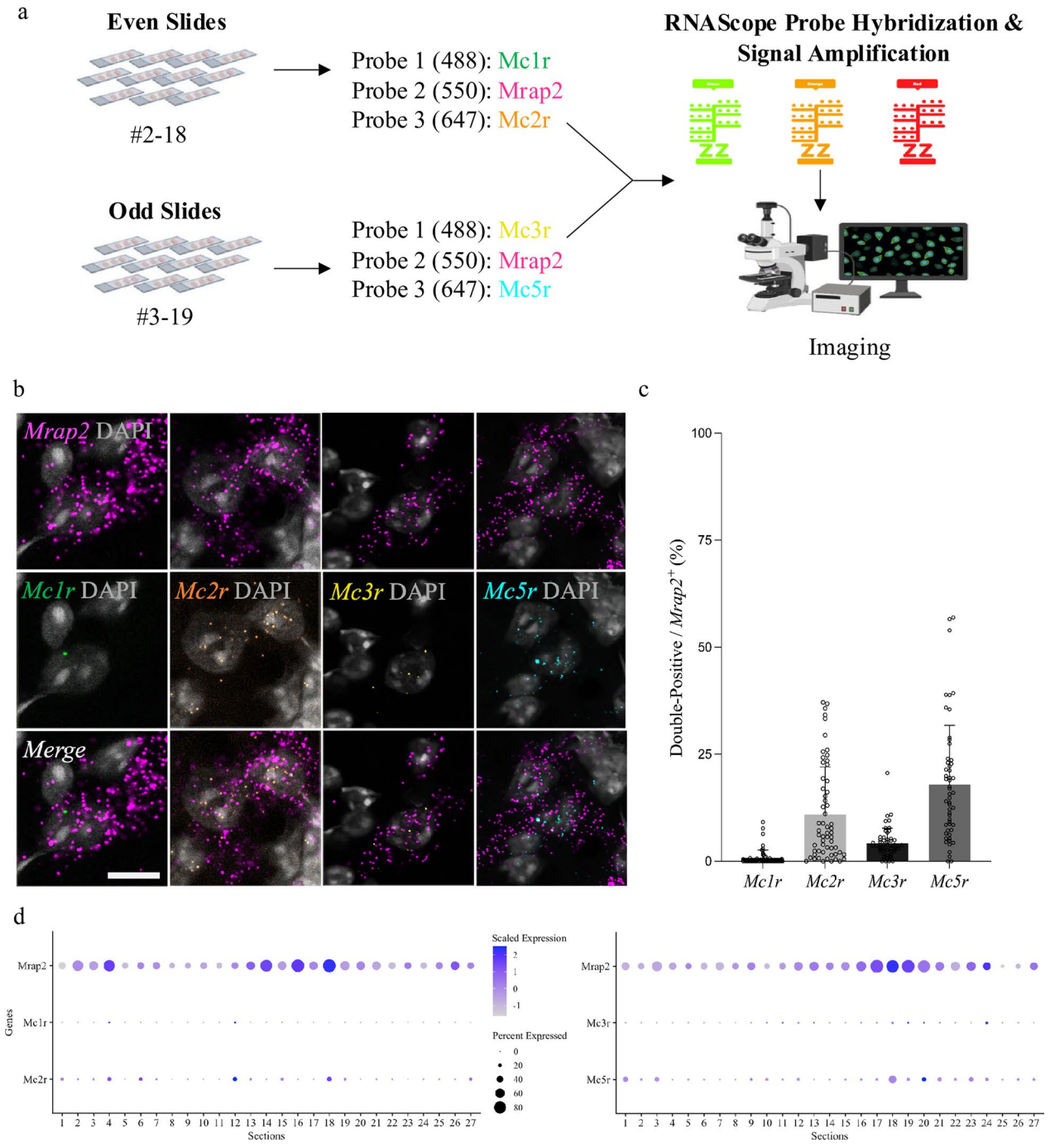

Fig. 6 RNAScope imaging of cells co-expressing *Mrap2, Mc1r, Mc2r, Mc3r,* and *Mc5r* in the LC. **a** Schematic diagram of RNAscope Multiplex experiment. Even and odd numbered slides were separated. Even slides were probed for *Mrap2, Mc1r,* and *Mc2r* and fluorescently labeled. Odd slides were probed for *Mrap2, Mc3r,* and *Mc5r* and fluorescently labeled. All slides were then imaged with the confocal microscope. **b** Cells were counterstained with DAPI (gray). Genes of interest were detected with fluorescent labeled probes and imaged. Magnification × 63. Scale Bar = 10 µm. **c** Bar graphs represent quantification of double-positive/*Mrap2*$^+$ cells, expressed as a percentage with individual data points for each section value. Data are means +/− SD. **d** Dot plot graphs showing expression levels of *Mrap2, Mc1r,* and *Mc2r* (left; even slides) and *Mrap2, Mc3r,* and *Mc5r* (right; odd slides). The size of the dot suggests the proportion of *Mrap2*$^+$ cells co-expressing each gene of interest. The spectrum of colors indicates the mean expression level. Section 1 is the most rostral section and section 27 is the most caudal section

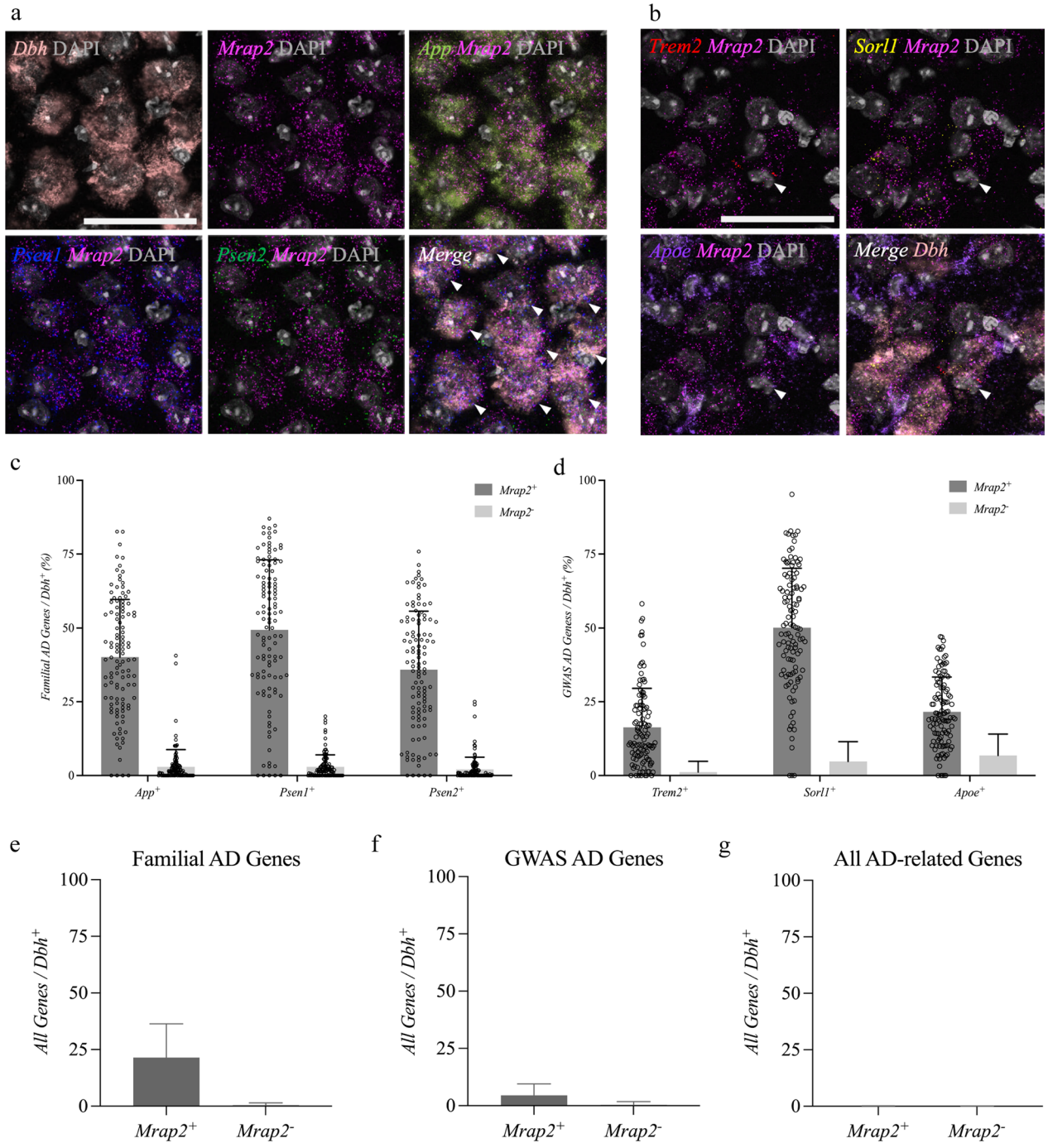

Fig. 7 RNAScope imaging of cells co-expressing *Mrap2* and AD-related genes in the LC. **a**–**b** Cells were counterstained with DAPI (gray). Familial AD Genes-*App, Psen1, Psen2*-and *Mrap2* were detected with fluorescent labeled probes and imaged in **a**. GWAS AD Genes-*Trem2, Sorl1, Apoe*-and *Mrap2* were detected with fluorescent labeled probes and imaged in **b**. Merged images in final panels. Magnification × 63. Scale Bar = 50 µm. **c**–**d** Bar graphs representing quantification of triple-positive cells expressed as a percentage of Dbh^+ cells with individual data points for each section value. $Mrap2^+$ and $Mrap2^-$ cell populations are represented. **e**–**g** Bar graphs represent quantification of cell populations co-expressing Familial AD genes in **e**, GWAS AD genes in **f**, and all AD related genes in **g**. Cell populations that were $Mrap2^+$ or $Mrap2^-$ were compared

through the suppression of inflammatory mediators, regulation of microglial motility, and reduction of oxidative stress [127–129]. In AD, the hypothalamus contains amyloid deposition and plaque formation [18, 20, 130, 131]. LC NE neurons project to the hypothalamus and damage to the LC is associated with atrophy and neuronal loss in the paraventricular and supraoptic nucleus of the hypothalamus, a process which may be mediated by

neuroinflammation [10, 132–134]. *Mrap2* is expressed throughout the hypothalamus and has been linked genetically to obesity [88, 135, 136]. Obesity is considered a chronic, low grade inflammatory state and it is a key risk factor for AD possibly through alterations in leptin signaling [62]. While mediators of leptin signaling have been implicated in AD, *MRAP2* may also serve as a potential link between the LC and the hypothalamus in AD pathogenesis.

Identification of AD-associated genes and *MRAP2* abundantly expressed within the LC is important as the LC had been implicated in both neurodegeneration and feeding dynamics [10, 14, 16, 17, 73]. There is significant cross species homology with regards to LC cellular organization, with some variation in neuronal abundance in some cellular subtypes of LC neurons between primates and rodents [64, 137]. Comparison of expression patterns using RNAscope in human samples would be valuable. The available brain tissue for our human studies consisted of female and male research subjects. However, due to the limited availability of female donors ($n = 1$ for snRNA-seq, $n = 1$ for Visium), sex specific analysis could not be performed. Anatomical and systems-level studies indicate that the core organization of the LC and its major afferent inputs, including hypothalamic projections, are conserved across sexes, with no evidence for qualitative sex differences in the presence or directionality of these pathways [26, 138, 139]. Thus, sex is as an important modulator of LC function that may influence the magnitude or behavioral consequences of noradrenergic signaling. While the underlying circuitry examined here is likely to be shared across sexes, lack of sex specific analysis is a limitation of this study.

Further, using HiPlex RNAscope and Multiplex RNAscope in mice ($n = 1$ for each assay) we generated complete, high-resolution anatomical maps, which has not been achieved previously. A limitation of this study is that it does not capture inter-animal variability or support statistical inference. Another consideration is that we do not make comparisons across age ranges in this study. Five-week-old mice are generally considered to be in mid adolescence (which is well beyond weaning). At this stage, the core anatomical organization of the melanocortin system including POMC and AgRP neuronal populations and their major projection patterns has already been established [140–142]. The melanocortin circuitry continues to mature, however, previous studies have demonstrated that expression of key melanocortin components such as *Pomc*, *Agrp*, and *Mc4r* is robust and readily detectable by 5-weeks of age [143–145].

Our study of human and mouse LC used spatially resolved transcriptomics, snRNA-seq, and RNAscope. Here we established the molecular characteristics of AD-related genes in the LC and identified a potential association with genes related to energy homeostasis via identification of cellular populations co-expressing *Mrap2* and AD-associated genes. Currently there are gaps in the literature regarding the characterization of melanocortin pathway genes and AD-related genes in the LC of individuals with AD relative to individuals without AD. Further studies of the effect of MRAP2 loss- and gain-of-function on gene expression in the LC and on AD pathology are needed to understand the impact on AD disease progression [67].

Supplementary Information

The online version contains supplementary material available at https://doi.org/10.1186/s40478-026-02287-x.

Additional file1. Supplementary Fig. 1 Meta-analysis of human LC snRNA-seq datasets.UMAP representation of all nuclei after integration, colored by dataset, shows extensive overlap of Basak, Weber and Siletti samples, indicating successful batch correction across studies.Violin plots summarizing quality-control metricsfor major neuronal and non-neuronal classes, stratified by dataset.Neuronal nuclei were subsetted from the integrated object and reintegrated, yielding 68 transcriptionally distinct neuronal subtypes that are visualized on UMAP and labeled according to characteristic gene expression profiles.Dot plot showing expression of top marker gene pairs used to define and annotate neuronal subtypes in c. Each row corresponds to a gene pair–defined subtype, and each column to an individual marker gene. Dot size indicates the percentage of nuclei expressing each gene within a subtype, while color intensity reflects scaled expression.Dot plot illustrating expression of selected noradrenergic markers, melanocortin pathway components and AD–related genes across neuronal subtypes and major non-neuronal cell classes

Additional file2. Supplementary Fig. 2 Integration of Basak and Weber Visium datasets in human LC.UMAP representation of all Visium spots colored by dataset shows substantial overlap between Basakand Weber sections after integration.UMAP colored by cell-type annotation demonstrates well-separated transcriptional clusters corresponding to NE neurons and additional neuronal and non-neuronal populations. Because each Visium spot contains RNA from multiple cells, these annotations represent cell-type–enriched spots rather than individual cells. The table summarizes spot numbers per annotated cell type in each dataset.Dot plot of canonical marker genes used for Visium cell-type assignment. Dot size reflects the percentage of spots expressing each gene within a given cell type, and color intensity indicates scaled expression. As in b, cell-type labels refer to spots enriched for a given cell class, not single cells.Violin plots summarize quality-control metricsfor each annotated cell type, stratified by dataset

Additional file3. Supplementary Fig. 3 Spatial distribution of Visium cell type–enriched annotations and gene expression.Cell-type annotations projected onto individual Visium sections from both datasets. Each spot is colored by its assigned cell type. Because each Visium spot contains RNA from multiple cells, these labels indicate spots enriched for a given cell class rather than individual cells.Spatial expression maps of DBH and SLC6A2, melanocortin pathway genes and selected AD–related genes on the same sections, illustrating their spatial distribution and relative expression levels across Basak and Weber samples. Color scales represent normalized expression levels

Additional file4. Supplementary Fig. 4 Mouse LC Identification in HALOwith random forest classifier.Selection of two background regions in red and two regions classified using Dbh as a marker for the LCin green. Scale Bar=500 µm.Real-time tuning of entire section based on Background and Dbh-LC selection criteria.Generation of annotation layer using random forest classifier function in HALO

Additional file5. Supplementary Fig. 5 Generation of thresholds for each gene of interest within the mouse LC.Overview of LC region from section 35, annotation layer was identified using random forest classifier in

HALO, Representative region for quantification was selected within the annotated LC region and outside of the annotated LC region and outlined in white using the square tool. Scale Bar=500 µm.Expression of genes of interest from the selected quantification region outside the Dbh-LC annotation region from section 35 is represented. Scale Bar=10 µm.Expression of genes of interest from the selected quantification region within the Dbh-LC annotation region from section 35 is represented. Scale Bar=10 µm.Quantification of the expression level of all genes within the outlined regions inside and outside the Dbh-LC annotation layer was completed using HALO. The minimum average number of molecules per cell for each gene of interest, as calculated from the left and right sides of three representative sections, is represented in the corresponding Bar Graph. Data are means +/−SD

Additional file6. Supplementary Fig. 6 Identification of mouse Mrap2^{+} cells which do not co-express Mc1r-Mc5r using RNAScope Hiplex and RNAScope Multiplex v2 assays. Percentage of Mrap2^{+} which were Mrap2^{+}Mc4r^{-} cells were identified from initial RNAScope Hi-Plex experiment. Percentage of Mrap2^{+} which were Mrap2^{+}Mc1r^{-} or Mrap2^{+}Mc2r^{-}cells were identified from the even numbered slides from the RNAScope Multiplex v2 assay. Percentage of Mrap2^{+} which were Mrap2^{+}Mc3r^{-} or Mrap2^{+}Mc5r^{-}cells were identified from the odd numbered slides from the RNAScope Multiplex v2 assay. Data are means +/−SD.

Additional file7. Supplementary Fig. 7 GPCR expression across neuronal and non-neuronal populations in the human snRNA-seq meta-dataset. Dot plots summarizing expression of noradrenergic genesand the curated IUPHAR GPCR panel across NE neuron subtypes, other neuronal subtypes, oligodendrocytes, OPCs, astrocytes, ependymal cells, microglia, and vascular populations in the integrated Basak + Weber + Siletti snRNA-seq dataset. Each row corresponds to a neuronal or non-neuronal population, and each column to an individual GPCR gene; the full gene set is displayed across multiple pages. Dot size indicates the percentage of nuclei expressing a given gene within each population, and color intensity reflects scaled average expression

Additional file8. Supplementary Fig. 8 Spatial distribution of GPCR expression in the integrated human LC Visium dataset. Spatial feature plots showing expression of noradrenergic genesand the curated IUPHAR GPCR panel across all integrated LC Visium sections from Basak and Weber donors. For each gene, Visium spots are displayed in tissue coordinate space, with color intensity indicating normalized expression at each spot. The complete GPCR panel is presented across multiple pages

Additional file9. Supplementary Table 1 Data-driven quality-control thresholds for the Basak snRNA-seq dataset. Batch-aware QC settings used to filter low-quality nuclei in the Basak snRNA-seq dataset. Each row corresponds to a defined QC batch. For each batch, lowerand upperthresholds were estimated for the indicated QC metric indicated in the "metric" column: number of detected genes, total UMI counts, and mitochondrial read fraction. "valley_log2" reports the position of the density minimum in log2-transformed space used to guide threshold selection, and "method" indicates the algorithm or fallback rule used to determine the final cut-offs. These thresholds were applied to remove low-quality nuclei, as described in the Methods

Additional file10. Supplementary Table 2 Human LC snRNA-seq donors and samples included in the integrated meta-dataset. For each dataset, the table lists donor ID, age, sex, post-mortem interval, sample IDs, and the number of nuclei, neurons, and DBH* NE neuronsfor each sample. Donor-level and dataset-level totals are provided, as well as grand totals across all donorsused in the integrated snRNA-seq meta-analysis

Additional file11. Supplementary Table 3 Human LC Visium donors and sections included in the integrated spatial transcriptomic dataset. For each dataset, the table lists donor ID, age, sex, post-mortem interval, Visium section IDs, the number of spots, and the number of spots assigned to the NE neuron-enriched LC regionin each section. Donor-level and dataset-level totals are provided, as well as grand totals across all donorsused in the integrated Visium analyses

Acknowledgements
The studies described in this manuscript were conducted, in part, through a research collaboration with Regeneron Pharmaceuticals Inc.

Author contributions
C.A.D., A.B., and F.M.B.E. conceptualized the study. A.B., F.M.B.E., M.C.D.R., Z.D., V.O., H.J.G., R.R., G.H., J.C.M., H.B., Y.B., Q.S., B.C., C.A., D.F., B.C., H.X., H.R., P.A.W., C.R., M.W.S., J.Y.A., and A.F.T. generated data, conducted portions of the analysis, assisted with data interpretation, and participated in sample provision. A.B., F.M.B.E., and M.C.D.R. wrote the main manuscript text. A.B., R.L.L., L.O.Q., A.F.T., C.A.D. revised and helped prepare the manuscript. C.A.D. was tasked with funding acquisition. C.A.D. and A.F.T. supervised the project. All authors reviewed and approved the final manuscript.

Funding
This work was supported by New York Obesity Research Center, P30 DK026687-43 and DK52431-25. The snRNA-seq study was funded in part through the NIH/NCI Cancer Center Support Grant P30CA013696 and used the Genomics and High Throughput Screening Shared Resource. This work was supported by the National Center for Advancing Translational Sciences, National Institutes of Health, through Grant Number UL1TR001873.

Data availability
Data that support the findings of this study have been deposited to GEO.

Availability of data and materials
Raw snRNA-seq data (Cell Ranger output matrices) and processed Seurat objects (Basak snRNA-seq, meta-analysis all cells, and meta-analysis neurons) are deposited in NCBI GEO under accession GSE327442. Raw Visium spatial transcriptomics data (Space Ranger output matrices, tissue images, and spatial coordinates), along with the processed Seurat object from the integrated Basak and Weber et al. (2024) Visium dataset, are deposited under accession GSE327441.

Code availability
All code used to reproduce the snRNA-seq and Visium analyses and figures in this manuscript is available on GitHub: https://github.com/fmbetul/LC-melanocortin-analysis. Analyses were performed using R version 4.3.2 and Seurat version 5.0.1.

Declarations

Ethics approval and consent to participate
All autopsy materials were donated to Columbia by next of kin for both diagnostic and research purposes. Our IRB has designated our study "not human subject research." All animal care and experimental procedures followed the US National Institutes of Health and Animal Care and Use guidelines and were approved by the Columbia University Animal Care and Use Committee (IACUC). Animals were sacrificed according to Columbia University regulations using the appropriate protocol (#AC-AABF6552).

Consent for publication
Not applicable.

Competing interests
Q.S., M.W.S., and J.Y.A. are full-time employees of Regeneron Pharmaceuticals Inc.

Author details
[1]Department of Pediatrics, Division of Molecular Genetics, Columbia University Irving Medical Center, New York, NY, USA
[2]Naomi Berrie Diabetes Center, Columbia University Irving Medical Center, New York, NY, USA
[3]Key Laboratory of Neuroregeneration of Jiangsu and Ministry of Education, Co-Innovation Center of Neuroregeneration, Nantong University, Nantong 226001, Jiangsu, China
[4]Department of Neurobiology and Anatomy, Drexel University College of Medicine, Philadelphia, PA, USA
[5]Department of Pathology and Cell Biology, Columbia University Irving Medical Center, New York, NY, USA

[6]Regeneron Genetics Center, Regeneron Pharmaceuticals Inc., Tarrytown, NY 10591, USA
[7]Taub Institute, Columbia University Irving Medical Center, New York, NY, USA
[8]Department of Neurology, Columbia University Irving Medical Center, New York, NY, USA

Received: 26 August 2025 / Accepted: 23 March 2026
Published online: 04 April 2026

References

1. Forny-Germano L, De Felice FG, Vieira M (2018) The role of leptin and adiponectin in obesity-associated cognitive decline and Alzheimer's disease. Front Neurosci 12:1027. https://doi.org/10.3389/fnins.2018.01027
2. Nordestgaard LT, Tybjærg-Hansen A, Nordestgaard BG, Frikke-Schmidt R (2017) Body mass index and risk of Alzheimer's disease: a Mendelian randomization study of 399,536 individuals. J Clin Endocrinol Metab 102(7):2310–2320. https://doi.org/10.1210/jc.2017-00195
3. Luchsinger JA, Cheng D, Tang MX, Schupf N, Mayeux R (2012) Central obesity in the elderly is related to late-onset Alzheimer disease. Alzheimer Dis Assoc Disord 26(2):101–105. https://doi.org/10.1097/WAD.0b013e318222f0d4
4. Xu WL, Atti AR, Gatz M, Pedersen NL, Johansson B, Fratiglioni L (2011) Midlife overweight and obesity increase late-life dementia risk: a population-based twin study. Neurology 76(18):1568–1574. https://doi.org/10.1212/WNL.0b013e3182190d09
5. Chuang YF, An Y, Bilgel M, Wong DF, Troncoso JC, O'Brien RJ et al (2016) Midlife adiposity predicts earlier onset of Alzheimer's dementia, neuropathology and presymptomatic cerebral amyloid accumulation. Mol Psychiatry 21(7):910–915. https://doi.org/10.1038/mp.2015.129
6. Betts MJ, Kirilina E, Otaduy MCG, Ivanov D, Acosta-Cabronero J, Callaghan MF et al (2019) Locus coeruleus imaging as a biomarker for noradrenergic dysfunction in neurodegenerative diseases. Brain 142(9):2558–2571. https://doi.org/10.1093/brain/awz193
7. Guyton AC (2006) Text book of medical physiology. China
8. Aston-Jones G, Cohen JD (2005) An integrative theory of locus coeruleus-norepinephrine function: adaptive gain and optimal performance. Annu Rev Neurosci 28:403–450. https://doi.org/10.1146/annurev.neuro.28.061604.135709
9. Foote SL, Berridge CW (2019) New developments and future directions in understanding locus coeruleus-Norepinephrine (LC-NE) function. Brain Res 1709:81–84. https://doi.org/10.1016/j.brainres.2018.09.033
10. Giorgi FS, Galgani A, Puglisi-Allegra S, Limanaqi F, Busceti CL, Fornai F (2020) Locus Coeruleus and neurovascular unit: From its role in physiology to its potential role in Alzheimer's disease pathogenesis. J Neurosci Res 98(12):2406–2434. https://doi.org/10.1002/jnr.24718
11. Sara SJ, Bouret S (2012) Orienting and reorienting: the locus coeruleus mediates cognition through arousal. Neuron 76(1):130–141. https://doi.org/10.1016/j.neuron.2012.09.011
12. Poe GR, Foote S, Eschenko O, Johansen JP, Bouret S, Aston-Jones G et al (2020) Locus coeruleus: a new look at the blue spot. Nat Rev Neurosci 21(11):644–659. https://doi.org/10.1038/s41583-020-0360-9
13. Aston-Jones G, Waterhouse B (2016) Locus coeruleus: from global projection system to adaptive regulation of behavior. Brain Res 1645:75–78. https://doi.org/10.1016/j.brainres.2016.03.001
14. Sciolino NR, Hsiang M, Mazzone CM, Wilson LR, Plummer NW, Amin J et al (2022) Natural locus coeruleus dynamics during feeding. Sci Adv 8(33):eabn9134. https://doi.org/10.1126/sciadv.abn9134
15. Weinshenker D (2018) Long road to ruin: noradrenergic dysfunction in neurodegenerative disease. Trends Neurosci 41(4):211–223. https://doi.org/10.1016/j.tins.2018.01.010
16. Mather M, Harley CW (2016) The Locus coeruleus: essential for maintaining cognitive function and the aging brain. Trends Cogn Sci 20(3):214–226. https://doi.org/10.1016/j.tics.2016.01.001
17. Chalermpalanupap T, Weinshenker D, Rorabaugh JM (2017) Down but not out: the consequences of pretangle Tau in the locus coeruleus. Neural Plast 2017(1):7829507. https://doi.org/10.1155/2017/7829507
18. Braak H, Thal DR, Ghebremedhin E, Del Tredici K (2011) Stages of the pathologic process in Alzheimer disease: age categories from 1 to 100 years. J Neuropathol Exp Neurol 70(11):960–969. https://doi.org/10.1097/NEN.0b013e318232a379
19. Ishii M, Iadecola C (2015) Metabolic and non-cognitive manifestations of Alzheimer's disease: the hypothalamus as both culprit and target of pathology. Cell Metab 22(5):761–776. https://doi.org/10.1016/j.cmet.2015.08.016
20. Giorgi FS, Galgani A, Puglisi-Allegra S, Busceti CL, Fornai F (2021) The connections of Locus Coeruleus with hypothalamus: potential involvement in Alzheimer's disease. J Neural Transm 128(5):589–613. https://doi.org/10.1007/s00702-021-02338-8
21. Lechan RM, Toni R (2000) Functional anatomy of the hypothalamus and pituitary. In: Feingold KR, Anawalt B, Blackman MR, et al (eds.) Endotext. MDText.com, Inc. Copyright © 2000–2024, MDText.com, Inc.
22. Schwarz LA, Luo L (2015) Organization of the Locus coeruleus-norepinephrine System. Curr Biol 25(21):R1051–R1056. https://doi.org/10.1016/j.cub.2015.09.039
23. Sherin JE, Elmquist JK, Torrealba F, Saper CB (1998) Innervation of histaminergic tuberomammillary neurons by GABAergic and galaninergic neurons in the ventrolateral preoptic nucleus of the rat. J Neurosci 18(12):4705–4721. https://doi.org/10.1523/jneurosci.18-12-04705.1998
24. Lee HS, Kim MA, Waterhouse BD (2005) Retrograde double-labeling study of common afferent projections to the dorsal raphe and the nuclear core of the Locus coeruleus in the rat. J Comp Neurol 481(2):179–193. https://doi.org/10.1002/cne.20365
25. Ericson H, Blomqvist A, Köhler C (1989) Brainstem afferents to the tuberomammillary nucleus in the rat brain with special reference to monoaminergic innervation. J Comp Neurol 281(2):169–192. https://doi.org/10.1002/cne.902810203
26. Samuels ER, Szabadi E (2008) Functional neuroanatomy of the noradrenergic locus coeruleus: its roles in the regulation of arousal and autonomic function part I: principles of functional organisation. Curr Neuropharmacol 6(3):235–253. https://doi.org/10.2174/157015908785777229
27. Cedarbaum JM, Aghajanian GK (1978) Afferent projections to the rat locus coeruleus as determined by a retrograde tracing technique. J Comp Neurol 178(1):1–16. https://doi.org/10.1002/cne.901780102
28. Steininger TL, Gong H, McGinty D, Szymusiak R (2001) Subregional organization of preoptic area/anterior hypothalamic projections to arousal-related monoaminergic cell groups. J Comp Neurol 429(4):638–653
29. Aston-Jones G, Bloom FE (1981) Activity of norepinephrine-containing locus coeruleus neurons in behaving rats anticipates fluctuations in the sleep-waking cycle. J Neurosci 1(8):876–886. https://doi.org/10.1523/jneurosci.01-08-00876.1981
30. Valentino RJ, Van Bockstaele E (2008) Convergent regulation of locus coeruleus activity as an adaptive response to stress. Eur J Pharmacol 583(2):194–203. https://doi.org/10.1016/j.ejphar.2007.11.062
31. Reyes BAS, Valentino RJ, Xu G, Van Bockstaele EJ (2005) Hypothalamic projections to locus coeruleus neurons in rat brain. Eur J Neurosci 22(1):93–106. https://doi.org/10.1111/j.1460-9568.2005.04197.x
32. Jiang Z, Rajamanickam S, Justice NJ (2018) Local corticotropin-Releasing factor signaling in the hypothalamic paraventricular nucleus. J Neurosci 38(8):1874. https://doi.org/10.1523/JNEUROSCI.1492-17.2017
33. Kräuchi K, Wirz-Justice A, Morimasa T, Willener R, Feer H (1984) Hypothalamic alpha 2- and beta-adrenoceptor rhythms are correlated with circadian feeding: evidence from chronic methamphetamine treatment and withdrawal. Brain Res 321(1):83–90. https://doi.org/10.1016/0006-8993(84)90683-8
34. Capuano CA, Leibowitz SF, Barr GA (1992) The pharmaco-ontogeny of the perifornical lateral hypothalamic β2-adrenergic and dopaminergic receptor systems mediating epinephrine- and dopamine-induced suppression of feeding in the rat. Dev Brain Res 70(1):1–7. https://doi.org/10.1016/0165-3806(92)90098-h
35. Horvath TL, Peyron C, Diano S, Ivanov A, Aston-Jones G, Kilduff TS et al (1999) Hypocretin (orexin) activation and synaptic innervation of the locus coeruleus noradrenergic system. J Comp Neurol 415(2):145–159
36. España RA, Reis KM, Valentino RJ, Berridge CW (2005) Organization of hypocretin/orexin efferents to locus coeruleus and basal forebrain arousal-related structures. J Comp Neurol 481(2):160–178. https://doi.org/10.1002/cne.20369
37. Date Y, Ueta Y, Yamashita H, Yamaguchi H, Matsukura S, Kangawa K et al (1999) Orexins, orexigenic hypothalamic peptides, interact with autonomic, neuroendocrine and neuroregulatory systems. Proc Natl Acad Sci U S A 96(2):748–753. https://doi.org/10.1073/pnas.96.2.748
38. Rouault AAJ, Lee AA, Sebag JA (2017) Regions of MRAP2 required for the inhibition of orexin and prokineticin receptor signaling. Biochimica et Biophysica Acta (BBA)—Molecular Cell Research 1864(12):2322–2329. https://doi.org/10.1016/j.bbamcr.2017.09.008

39. Rouault AAJ, Rosselli-Murai LK, Hernandez CC, Gimenez LE, Tall GG, Sebag JA (2020) The GPCR accessory protein MRAP2 regulates both biased signaling and constitutive activity of the ghrelin receptor GHSR1a. Sci Signal. https://doi.org/10.1126/scisignal.aax4569
40. Rouault AAJ, Buscaglia P, Sebag JA (2022) MRAP2 inhibits β-arrestin recruitment to the ghrelin receptor by preventing GHSR1a phosphorylation. J Biol Chem 298(6):102057. https://doi.org/10.1016/j.jbc.2022.102057
41. Wang M, Zhai Y, Lei X, Xu J, Jiang B, Kuang Z et al (2022) Determination of the interaction and pharmacological modulation of MCHR1 signaling by the C-terminus of MRAP2 protein. Front Endocrinol (Lausanne) 13:848728. https://doi.org/10.3389/fendo.2022.848728
42. Zhang S, Wang P, Ji B, Shao Y, Hou S, Chen J et al (2025) Signal transduction, dimerization, and therapeutic targeting of orexin and receptor systems. Front Pharmacol 16:1697406. https://doi.org/10.3389/fphar.2025.1697406
43. Trivedi P, Yu H, MacNeil DJ, Van der Ploeg LH, Guan XM (1998) Distribution of orexin receptor mRNA in the rat brain. FEBS Lett 438(1–2):71–75. https://doi.org/10.1016/s0014-5793(98)01266-6
44. Marcus JN, Aschkenasi CJ, Lee CE, Chemelli RM, Saper CB, Yanagisawa M et al (2001) Differential expression of orexin receptors 1 and 2 in the rat brain. J Comp Neurol 435(1):6–25. https://doi.org/10.1002/cne.1190
45. Maric I, López-Ferreras L, Bhat Y, Asker M, Börchers S, Bellfy L et al (2023) From the stomach to locus coeruleus: new neural substrate for ghrelin's effects on ingestive, motivated and anxiety-like behaviors. Front Pharmacol 14:1286805. https://doi.org/10.3389/fphar.2023.1286805
46. Saito Y, Cheng M, Leslie FM, Civelli O (2001) Expression of the melanin-concentrating hormone (MCH) receptor mRNA in the rat brain. J Comp Neurol 435(1):26–40. https://doi.org/10.1002/cne.1191
47. Cone RD (2005) Anatomy and regulation of the central melanocortin system. Nat Neurosci 8(5):571–578. https://doi.org/10.1038/nn1455
48. Palkovits M, Mezey E, Eskay RL (1987) Pro-opiomelanocortin-derived peptides (ACTH/beta-endorphin/alpha-MSH) in brainstem baroreceptor areas of the rat. Brain Res 436(2):323–338. https://doi.org/10.1016/0006-8993(87)91676-3
49. Suzuki I, Cone RD, Im S, Nordlund J, Abdel-Malek ZA (1996) Binding of melanotropic hormones to the melanocortin receptor MC1R on human melanocytes stimulates proliferation and melanogenesis. Endocrinology 137(5):1627–1633. https://doi.org/10.1210/endo.137.5.8612494
50. Mountjoy KG, Robbins LS, Mortrud MT, Cone RD (1992) The cloning of a family of genes that encode the melanocortin receptors. Science 257(5074):1248–1251. https://doi.org/10.1126/science.1325670
51. Yuan XC, Tao YX (2022) Ligands for melanocortin receptors: beyond melanocyte-stimulating hormones and adrenocorticotropin. Biomolecules. https://doi.org/10.3390/biom12101407
52. D'Agostino G, Diano S (2010) Alpha-melanocyte stimulating hormone: production and degradation. J Mol Med (Berl) 88(12):1195–1201. https://doi.org/10.1007/s00109-010-0651-0
53. Krashes MJ, Lowell BB, Garfield AS (2016) Melanocortin-4 receptor-regulated energy homeostasis. Nat Neurosci 19(2):206–219. https://doi.org/10.1038/nn.4202
54. Mountjoy KG, Mortrud MT, Low MJ, Simerly RB, Cone RD (1994) Localization of the melanocortin-4 receptor (MC4-R) in neuroendocrine and autonomic control circuits in the brain. Mol Endocrinol 8(10):1298–1308. https://doi.org/10.1210/mend.8.10.7854347
55. Mountjoy KG (2010) Distribution and function of melanocortin receptors within the brain. Adv Exp Med Biol 681:29–48. https://doi.org/10.1007/978-1-4419-6354-3_3
56. Caruso V, Lagerström MC, Olszewski PK, Fredriksson R, Schiöth HB (2014) Synaptic changes induced by melanocortin signalling. Nat Rev Neurosci 15(2):98–110. https://doi.org/10.1038/nrn3657
57. Serova LI, Gueorguiev V, Cheng SY, Sabban EL (2008) Adrenocorticotropic hormone elevates gene expression for catecholamine biosynthesis in rat superior cervical ganglia and locus coeruleus by an adrenal independent mechanism. Neuroscience 153(4):1380–1389. https://doi.org/10.1016/j.neuroscience.2008.02.059
58. Liu H, Li X, Li P, Hai R, Li J, Fan Q et al (2023) Glutamatergic melanocortin-4 receptor neurons regulate body weight. FASEB J 37(5):e22920. https://doi.org/10.1096/fj.202201786R
59. Tartaglia LA, Dembski M, Weng X, Deng N, Culpepper J, Devos R et al (1995) Identification and expression cloning of a leptin receptor, OB-R. Cell 83(7):1263–1271. https://doi.org/10.1016/0092-8674(95)90151-5
60. Sebag JA, Zhang C, Hinkle PM, Bradshaw AM, Cone RD (2013) Developmental control of the melanocortin-4 receptor by MRAP2 proteins in zebrafish. Science 341(6143):278–281. https://doi.org/10.1126/science.1232995
61. Yeo GSH, Chao DHM, Siegert AM, Koerperich ZM, Ericson MD, Simonds SE et al (2021) The melanocortin pathway and energy homeostasis: from discovery to obesity therapy. Mol Metab 48:101206. https://doi.org/10.1016/j.molmet.2021.101206
62. Flores-Cordero JA, Pérez-Pérez A, Jiménez-Cortegana C, Alba G, Flores-Barragán A, Sánchez-Margalet V (2022) Obesity as a risk factor for dementia and Alzheimer's disease: The role of leptin. Int J Mol Sci. https://doi.org/10.3390/ijms23095202
63. Caramia M, Romanov RA, Sideromenos S, Hevesi Z, Zhao M, Krasniakova M et al (2023) Neuronal diversity of neuropeptide signaling, including galanin, in the mouse locus coeruleus. Proc Natl Acad Sci U S A 120(31):e2222095120. https://doi.org/10.1073/pnas.2222095120
64. Weber LM, Divecha HR, Tran MN, Kwon SH, Spangler A, Montgomery KD et al (2024) The gene expression landscape of the human locus coeruleus revealed by single-nucleus and spatially-resolved transcriptomics. Elife 12:84628. https://doi.org/10.7554/eLife.84628
65. Nardone S, De Luca R, Zito A, Klymko N, Nicoloutsopoulos D, Amsalem O et al (2024) A spatially-resolved transcriptional atlas of the murine dorsal pons at single-cell resolution. Nat Commun 15(1):1966. https://doi.org/10.1038/s41467-024-45907-7
66. Siletti K, Hodge R, Mossi Albiach A, Lee KW, Ding SL, Hu L et al (2023) Transcriptomic diversity of cell types across the adult human brain. Science 382(6667):eadd7046. https://doi.org/10.1126/science.add7046
67. Marques-Coelho D, Iohan LdCC, de Farias ARM, Flaig A, Letournel F, Martin-Négrier M-L et al (2021) Differential transcript usage unravels gene expression alterations in Alzheimer's disease human brains. npj Aging Mech Dis 7(1):2. https://doi.org/10.1038/s41514-020-00052-5
68. Bali J, Gheinani AH, Zurbriggen S, Rajendran L (2012) Role of genes linked to sporadic Alzheimer's disease risk in the production of β-amyloid peptides. Proc Natl Acad Sci U S A 109(38):15307–15311. https://doi.org/10.1073/pnas.1201632109
69. Bird TD (2008) Genetic aspects of Alzheimer disease. Genet Med 10(4):231–239. https://doi.org/10.1097/GIM.0b013e31816b64dc
70. Tanzi RE (2012) The genetics of Alzheimer disease. Cold Spring Harb Perspect Med. https://doi.org/10.1101/cshperspect.a006296
71. Price DL, Sisodia SS (1998) Mutant genes in familial Alzheimer's disease and transgenic models. Annu Rev Neurosci 21(1):479–505. https://doi.org/10.1146/annurev.neuro.21.1.479
72. Bertram L, Tanzi RE (2012) The genetics of Alzheimer's disease. Prog Mol Biol Transl Sci 107:79–100. https://doi.org/10.1016/b978-0-12-385883-2.00008-4
73. Mercan D, Heneka MT (2022) The contribution of the locus coeruleus-noradrenaline system degeneration during the progression of Alzheimer's disease. Biology (Basel). https://doi.org/10.3390/biology11121822
74. Cruts M, van Duijn CM, Backhovens H, Van den Broeck M, Wehnert A, Serneels S et al (1998) Estimation of the genetic contribution of presenilin-1 and -2 mutations in a population-based study of presenile Alzheimer disease. Hum Mol Genet 7(1):43–51. https://doi.org/10.1093/hmg/7.1.43
75. Yin RH, Yu JT, Tan L (2015) The role of SORL1 in Alzheimer's disease. Mol Neurobiol 51(3):909–918. https://doi.org/10.1007/s12035-014-8742-5
76. Campion D, Charbonnier C, Nicolas G (2019) SORL1 genetic variants and Alzheimer disease risk: a literature review and meta-analysis of sequencing data. Acta Neuropathol 138(2):173–186. https://doi.org/10.1007/s00401-019-01991-4
77. Bøgh N, Sørensen CB, Alstrup AKO, Hansen ESS, Andersen OM, Laustsen C (2024) Mice and minipigs with compromised expression of the Alzheimer's disease gene SORL1 show cerebral metabolic disturbances on hyperpolarized [1-13C]pyruvate and sodium MRI. Brain Commun. https://doi.org/10.1093/braincomms/fcae114
78. DeMattos RB, Cirrito JR, Parsadanian M, May PC, O'Dell MA, Taylor JW et al (2004) ApoE and clusterin cooperatively suppress Abeta levels and deposition: evidence that ApoE regulates extracellular Abeta metabolism in vivo. Neuron 41(2):193–202. https://doi.org/10.1016/s0896-6273(03)00850-x
79. Strobel S, Grünblatt E, Riederer P, Heinsen H, Arzberger T, Al-Sarraj S et al (2015) Changes in the expression of genes related to neuroinflammation over the course of sporadic Alzheimer's disease progression: CX3CL1, TREM2, and PPARγ. J Neural Transm 122(7):1069–1076. https://doi.org/10.1007/s00702-015-1369-5
80. Jay TR, von Saucken VE, Landreth GE (2017) TREM2 in neurodegenerative diseases. Mol Neurodegener 12(1):56. https://doi.org/10.1186/s13024-017-0197-5

81. Guerreiro R, Wojtas A, Bras J, Carrasquillo M, Rogaeva E, Majounie E et al (2013) TREM2 variants in Alzheimer's disease. N Engl J Med 368(2):117–127. https://doi.org/10.1056/NEJMoa1211851
82. Delizannis AT, Nonneman A, Tsering W, De Bondt A, Van den Wyngaert I, Zhang B et al (2021) Effects of microglial depletion and TREM2 deficiency on Aβ plaque burden and neuritic plaque tau pathology in 5XFAD mice. Acta Neuropathol Commun 9(1):150. https://doi.org/10.1186/s40478-021-01251-1
83. Hao Y, Stuart T, Kowalski MH, Choudhary S, Hoffman P, Hartman A et al (2024) Dictionary learning for integrative, multimodal and scalable single-cell analysis. Nat Biotechnol 42(2):293–304. https://doi.org/10.1038/s41587-023-01767-y
84. Harding SD, Armstrong JF, Faccenda E, Southan C, Alexander SPH, Davenport AP et al (2026) The IUPHAR/BPS guide to pharmacology in 2026. Nucleic Acids Res 54(D1):D1446–D1456. https://doi.org/10.1093/nar/gkaf1067
85. Alexander SPH, Davenport AP, Kelly E, Gibb AJ, Mathie AA, Peach CJ et al (2025) The concise guide to pharmacology 2025/26: G protein-coupled receptors. Br J Pharmacol 182(Suppl 1):S24-s151. https://doi.org/10.1111/bph.70230
86. Mulvey B, Bhatti DL, Gyawali S, Lake AM, Kriaucionis S, Ford CP et al (2018) Molecular and functional sex differences of noradrenergic neurons in the mouse locus coeruleus. Cell Rep 23(8):2225–2235. https://doi.org/10.1016/j.celrep.2018.04.054
87. Sutin EL, Jacobowitz DM (1991) Chapter 1—Neurochemicals in the dorsal pontine tegmentum. In: Barnes CD, Pompeiano O (eds) Progress in Brain Research. Elsevier, pp 3–14
88. Chan LF, Webb TR, Chung T-T, Meimaridou E, Cooray SN, Guasti L et al (2009) MRAP and MRAP2 are bidirectional regulators of the melanocortin receptor family. Proc Natl Acad Sci U S A 106(15):6146–6151. https://doi.org/10.1073/pnas.0809918106
89. Kiliaan AJ, Arnoldussen IA, Gustafson DR (2014) Adipokines: a link between obesity and dementia? Lancet Neurol 13(9):913–923. https://doi.org/10.1016/s1474-4422(14)70085-7
90. Lloret A, Monllor P, Esteve D, Cervera-Ferri A, Lloret MA (2019) Obesity as a risk factor for Alzheimer's Disease: implication of leptin and glutamate. Front Neurosci 13:508. https://doi.org/10.3389/fnins.2019.00508
91. Arnoldussen IAC, Kiliaan AJ, Gustafson DR (2014) Obesity and dementia: adipokines interact with the brain. Eur Neuropsychopharmacol 24(12):1982–1999. https://doi.org/10.1016/j.euroneuro.2014.03.002
92. Holden KF, Lindquist K, Tylavsky FA, Rosano C, Harris TB, Yaffe K (2009) Serum leptin level and cognition in the elderly: findings from the Health ABC Study. Neurobiol Aging 30(9):1483–1489. https://doi.org/10.1016/j.neurobiolaging.2007.11.024
93. Ishii A, Furusho M, Dupree JL, Bansal R (2014) Role of ERK1/2 MAPK signaling in the maintenance of myelin and axonal integrity in the adult CNS. J Neurosci 34(48):16031–16045. https://doi.org/10.1523/jneurosci.3360-14.2014
94. Chan-Palay V, Asan E (1989) Quantitation of catecholamine neurons in the locus coeruleus in human brains of normal young and older adults and in depression. J Comp Neurol 287(3):357–372. https://doi.org/10.1002/cne.902870307
95. Chandler DJ, Jensen P, McCall JG, Pickering AE, Schwarz LA, Totah NK (2019) Redefining noradrenergic neuromodulation of behavior: impacts of a modular locus coeruleus architecture. J Neurosci 39(42):8239–8249. https://doi.org/10.1523/jneurosci.1164-19.2019
96. Plummer NW, Scappini EL, Smith KG, Tucker CJ, Jensen P (2017) Two subpopulations of noradrenergic neurons in the locus coeruleus complex distinguished by expression of the dorsal neural tube marker Pax7. Front Neuroanat 11:60. https://doi.org/10.3389/fnana.2017.00060
97. Jiang J, Wang C, Qi R, Fu H, Ma Q (2020) scREAD: a single-cell RNA-Seq database for Alzheimer's disease. iScience 23(11):101769. https://doi.org/10.1016/j.isci.2020.101769
98. Macosko EZ, Basu A, Satija R, Nemesh J, Shekhar K, Goldman M et al (2015) Highly parallel genome-wide expression profiling of individual cells using nanoliter droplets. Cell 161(5):1202–1214. https://doi.org/10.1016/j.cell.2015.05.002
99. Ma HT, Zhang HC, Zuo ZF, Liu YX (2023) Heterogeneous organization of Locus coeruleus: an intrinsic mechanism for functional complexity. Physiol Behav 268:114231. https://doi.org/10.1016/j.physbeh.2023.114231
100. Laque A, Yu S, Qualls-Creekmore E, Gettys S, Schwartzenburg C, Bui K et al (2015) Leptin modulates nutrient reward via inhibitory galanin action on orexin neurons. Molecular Metabolism 4(10):706–717. https://doi.org/10.1016/j.molmet.2015.07.002
101. Asai M, Ramachandrappa S, Joachim M, Shen Y, Zhang R, Nuthalapati N et al (2013) Loss of function of the melanocortin 2 receptor accessory protein 2 is associated with mammalian obesity. Science 341(6143):275–278. https://doi.org/10.1126/science.1233000
102. Geets E, Zegers D, Beckers S, Verrijken A, Massa G, Van Hoorenbeeck K et al (2016) Copy number variation (CNV) analysis and mutation analysis of the 6q14.1-6q16.3 genes SIM1 and MRAP2 in Prader Willi like patients. Mol Genet Metab 117(3):383–388. https://doi.org/10.1016/j.ymgme.2016.01.003
103. Schonnop L, Kleinau G, Herrfurth N, Volckmar AL, Cetindag C, Müller A et al (2016) Decreased melanocortin-4 receptor function conferred by an infrequent variant at the human melanocortin receptor accessory protein 2 gene. Obesity 24(9):1976–1982. https://doi.org/10.1002/oby.21576
104. Jamaluddin A, Wyatt RA, Lee J, Dowsett GKC, Tadross JA, Broichhagen J et al. (2024) The MRAP2 accessory protein directly interacts with melanocortin-3 receptor to enhance signaling. bioRxiv. 2024: 11.06.622243. https://doi.org/10.1101/2024.11.06.622243
105. Bernard A, Ojeda Naharros I, Yue X, Mifsud F, Blake A, Bourgain-Guglielmetti F et al (2023) MRAP2 regulates energy homeostasis by promoting primary cilia localization of MC4R. JCI Insight. https://doi.org/10.1172/jci.insight.155900
106. Baron M, Maillet J, Huyvaert M, Dechaume A, Boutry R, Loiselle H et al (2019) Loss-of-function mutations in MRAP2 are pathogenic in hyperphagic obesity with hyperglycemia and hypertension. Nat Med 25(11):1733–1738. https://doi.org/10.1038/s41591-019-0622-0
107. Bruschetta G, Kim JD, Diano S, Chan LF (2018) Overexpression of melanocortin 2 receptor accessory protein 2 (MRAP2) in adult paraventricular MC4R neurons regulates energy intake and expenditure. Mol Metab 18:79–87. https://doi.org/10.1016/j.molmet.2018.09.010
108. Wang M, Wang X, Jiang B, Zhai Y, Zheng J, Yang L et al (2022) Identification of MRAP protein family as broad-spectrum GPCR modulators. Clin Transl Med 12(11):e1091. https://doi.org/10.1002/ctm2.1091
109. Zitnik GA (2016) Control of arousal through neuropeptide afferents of the locus coeruleus. Brain Res 1641(Pt B):338–350. https://doi.org/10.1016/j.brainres.2015.12.010
110. Harris FM, Tesseur I, Brecht WJ, Xu Q, Mullendorff K, Chang S et al (2004) Astroglial regulation of apolipoprotein E expression in neuronal cells. Implications for Alzheimer's disease. J Biol Chem 279(5):3862–3868
111. Bekris LM, Yu C-E, Bird TD, Tsuang D (2011) The Genetics of Alzheimer's disease and Parkinson's disease. In: Blass JP (ed) Neurochemical mechanisms in disease. New York, Springer, pp 695–755
112. Kelly SC, He B, Perez SE, Ginsberg SD, Mufson EJ, Counts SE (2017) Locus coeruleus cellular and molecular pathology during the progression of Alzheimer's disease. Acta Neuropathol Commun 5(1):8. https://doi.org/10.1186/s40478-017-0411-2
113. Jonsson T, Stefansson H, Steinberg S, Jonsdottir I, Jonsson PV, Snaedal J et al (2013) Variant of TREM2 associated with the risk of Alzheimer's disease. N Engl J Med 368(2):107–116. https://doi.org/10.1056/NEJMoa1211103
114. Hickman SE, El Khoury J (2014) TREM2 and the neuroimmunology of Alzheimer's disease. Biochem Pharmacol 88(4):495–498. https://doi.org/10.1016/j.bcp.2013.11.021
115. Lue LF, Schmitz CT, Serrano G, Sue LI, Beach TG, Walker DG (2015) TREM2 protein expression changes correlate with Alzheimer's disease neurodegenerative pathologies in post-mortem temporal cortices. Brain Pathol 25(4):469–480. https://doi.org/10.1111/bpa.12190
116. Frank S, Burbach GJ, Bonin M, Walter M, Streit W, Bechmann I et al (2008) TREM2 is upregulated in amyloid plaque-associated microglia in aged APP23 transgenic mice. Glia 56(13):1438–1447. https://doi.org/10.1002/glia.20710
117. Hsieh CL, Koike M, Spusta SC, Niemi EC, Yenari M, Nakamura MC et al (2009) A role for TREM2 ligands in the phagocytosis of apoptotic neuronal cells by microglia. J Neurochem 109(4):1144–1156. https://doi.org/10.1111/j.1471-4159.2009.06042.x
118. Kiialainen A, Hovanes K, Paloneva J, Kopra O, Peltonen L (2005) Dap12 and Trem2, molecules involved in innate immunity and neurodegeneration, are co-expressed in the CNS. Neurobiol Dis 18(2):314–322. https://doi.org/10.1016/j.nbd.2004.09.007
119. Neumann H, Takahashi K (2007) Essential role of the microglial triggering receptor expressed on myeloid cells-2 (TREM2) for central nervous tissue immune homeostasis. J Neuroimmunol 184(1–2):92–99. https://doi.org/10.1016/j.jneuroim.2006.11.032
120. Prada I, Ongania GN, Buonsanti C, Panina-Bordignon P, Meldolesi J (2006) Triggering receptor expressed in myeloid cells 2 (TREM2) trafficking in microglial cells: continuous shuttling to and from the plasma membrane regulated by

cell stimulation. Neuroscience 140(4):1139–1148. https://doi.org/10.1016/j.neuroscience.2006.03.058
121. Schmid CD, Sautkulis LN, Danielson PE, Cooper J, Hasel KW, Hilbush BS et al (2002) Heterogeneous expression of the triggering receptor expressed on myeloid cells-2 on adult murine microglia. J Neurochem 83(6):1309–1320. https://doi.org/10.1046/j.1471-4159.2002.01243.x
122. Sessa G, Podini P, Mariani M, Meroni A, Spreafico R, Sinigaglia F et al (2004) Distribution and signaling of TREM2/DAP12, the receptor system mutated in human polycystic lipomembraneous osteodysplasia with sclerosing leukoencephalopathy dementia. Eur J Neurosci 20(10):2617–2628. https://doi.org/10.1111/j.1460-9568.2004.03729.x
123. Takahashi K, Rochford CD, Neumann H (2005) Clearance of apoptotic neurons without inflammation by microglial triggering receptor expressed on myeloid cells-2. J Exp Med 201(4):647–657. https://doi.org/10.1084/jem.20041611
124. Verloes A, Maquet P, Sadzot B, Vivario M, Thiry A, Franck G (1997) Nasu-Hakola syndrome: polycystic lipomembranous osteodysplasia with sclerosing leucoencephalopathy and presenile dementia. J Med Genet 34(9):753–757. https://doi.org/10.1136/jmg.34.9.753
125. Colonna M (2003) TREMs in the immune system and beyond. Nat Rev Immunol 3(6):445–453. https://doi.org/10.1038/nri1106
126. Kono J, Konno K, Talukder AH, Fuse T, Abe M, Uchida K et al (2017) Distribution of corticotropin-releasing factor neurons in the mouse brain: a study using corticotropin-releasing factor-modified yellow fluorescent protein knock-in mouse. Brain Struct Funct 222(4):1705–1732. https://doi.org/10.1007/s00429-016-1303-0
127. Beardmore R, Hou R, Darekar A, Holmes C, Boche D (2021) The Locus Coeruleus in aging and Alzheimer's Disease: A postmortem and brain imaging review. J Alzheimers Dis 83(1):5–22. https://doi.org/10.3233/jad-210191
128. Gyoneva S, Traynelis SF (2013) Norepinephrine modulates the motility of resting and activated microglia via different adrenergic receptors. J Biol Chem 288(21):15291–15302. https://doi.org/10.1074/jbc.M113.458901
129. Marien MR, Colpaert FC, Rosenquist AC (2004) Noradrenergic mechanisms in neurodegenerative diseases: a theory. Brain Res Rev 45(1):38–78. https://doi.org/10.1016/j.brainresrev.2004.02.002
130. Hiller AJ, Ishii M (2018) Disorders of body weight, sleep and circadian rhythm as manifestations of hypothalamic dysfunction in Alzheimer's Disease. Front Cell Neurosci 12:471. https://doi.org/10.3389/fncel.2018.00471
131. Thal DR, Rüb U, Orantes M, Braak H (2002) Phases of A beta-deposition in the human brain and its relevance for the development of AD. Neurology 58(12):1791–1800. https://doi.org/10.1212/wnl.58.12.1791
132. Farley IJ, Hornykiewicz O (1977) Noradrenaline distribution insubcortical areas of the human brain. Brain Res 126(1):53–62. https://doi.org/10.1016/0006-8993(77)90214-1
133. Bowden DM, German DC, Poynter DW (1978) An autoradiographic, semistereotaxic mapping of major projections from locus coeruleus and adjacent nuclei in Macaca mulatta. Brain Res 145(2):257–276. https://doi.org/10.1016/0006-8993(78)90861-2
134. Mann DM, Yates PO, Marcyniuk B (1985) Changes in Alzheimer's disease in the magnocellular neurones of the supraoptic and paraventricular nuclei of the hypothalamus and their relationship to the noradrenergic deficit. Clin Neuropathol 4(3):127–134
135. Berruien NNA, Smith CL (2020) Emerging roles of melanocortin receptor accessory proteins (MRAP and MRAP2) in physiology and pathophysiology. Gene 757:144949. https://doi.org/10.1016/j.gene.2020.144949
136. Srisai D, Yin TC, Lee AA, Rouault AAJ, Pearson NA, Grobe JL et al (2017) MRAP2 regulates ghrelin receptor signaling and hunger sensing. Nat Commun 8(1):713. https://doi.org/10.1038/s41467-017-00747-6
137. Manger PR, Eschenko O (2021) The mammalian locus coeruleus complex-consistencies and variances in nuclear organization. Brain Sci. https://doi.org/10.3390/brainsci11111486
138. Luppi PH, Aston-Jones G, Akaoka H, Chouvet G, Jouvet M (1995) Afferent projections to the rat locus coeruleus demonstrated by retrograde and anterograde tracing with cholera-toxin B subunit and Phaseolus vulgaris leucoagglutinin. Neuroscience 65(1):119–160. https://doi.org/10.1016/0306-4522(94)00481-J
139. Schwarz LA, Miyamichi K, Gao XJ, Beier KT, Weissbourd B, DeLoach KE et al (2015) Viral-genetic tracing of the input–output organization of a central noradrenaline circuit. Nature 524(7563):88–92. https://doi.org/10.1038/nature14600
140. Coupe B, Bouret SG (2013) Development of the hypothalamic melanocortin system. Front Endocrinol 4:38. https://doi.org/10.3389/fendo.2013.00038
141. Bouret SG, Draper SJ, Simerly RB (2004) Formation of projection pathways from the arcuate nucleus of the hypothalamus to hypothalamic regions implicated in the neural control of feeding behavior in mice. J Neurosci 24(11):2797–2805. https://doi.org/10.1523/jneurosci.5369-03.2004
142. Padilla SL, Carmody JS, Zeltser LM (2010) Pomc-expressing progenitors give rise to antagonistic neuronal populations in hypothalamic feeding circuits. Nat Med 16(4):403–405. https://doi.org/10.1038/nm.2126
143. Lieu L, Chau D, Afrin S, Dong Y, Alhadeff AL, Betley JN et al (2020) Effects of metabolic state on the regulation of melanocortin circuits. Physiol Behav 224:113039. https://doi.org/10.1016/j.physbeh.2020.113039
144. Nelson JF, Bender M, Schachter BS (1988) Age-related changes in proopiomelanocortin messenger ribonucleic acid levels in hypothalamus and pituitary of female C57BL/6J mice. Endocrinology 123(1):340–344. https://doi.org/10.1210/endo-123-1-340
145. Arens J, Moar KM, Eiden S, Weide K, Schmidt I, Mercer JG et al (2003) Age-dependent hypothalamic expression of neuropeptides in wild-type and melanocortin-4 receptor-deficient mice. Physiol Genomics 16(1):38–46. https://doi.org/10.1152/physiolgenomics.00123.2003

Publisher's Note